Journal of Materials Chemistry A

REVIEW

View Article Online
View Journal | View Issue

Cite this: J. Mater. Chem. A, 2015, 3, 18809

Perovskites for photovoltaics: a combined review of organic–inorganic halide perovskites and ferroelectric oxide perovskites

Zhen Fan,[ab] Kuan Sun[c] and John Wang*[a]

Received 11th June 2015
Accepted 15th July 2015

DOI: 10.1039/c5ta04235f

www.rsc.org/MaterialsA

Over the past few years, very interestingly, two subclasses of perovskites — organic–inorganic halide perovskites and ferroelectric oxide perovskites, have simultaneously become the hotspots in the research field of photovoltaics. Organic–inorganic halide perovskites have launched a new era of low-cost, high-efficiency solar cells, due to their easy solution processability and superior optical and electrical properties for the photovoltaic effect. More recently, a so-called giant switchable photovoltaic effect has been demonstrated in organic–inorganic halide perovskites, thus promising a new memristive functionality. On the other hand, the recent renaissance of ferroelectric oxide perovskites for photovoltaics is caused by their fundamentally new photovoltaic mechanisms, which can produce a photovoltage far beyond the bandgap and may even lead to a boost of energy conversion efficiency. In addition, the combination of photovoltaic properties with the ferroic orders may create many novel functionalities for ferroelectric oxide perovskites. Toward the common goals of developing high-efficiency photovoltaics and novel opto-electronic functional devices, these two different subclasses of perovskites shall be brought together into a combined review. In this context, we review both organic–inorganic halide perovskites and ferroelectric oxide perovskites for photovoltaics, focusing on the material nature and the photovoltaic mechanisms. We also discuss their respective unresolved issues, along with useful suggestions for future research.

1. Introduction

With the sun providing abundant, clean, and renewable energy constantly, how to utilize the solar energy in an effective and low-cost manner is both attractive and also challenging for the human society. One important way to harvest solar energy is known as the photovoltaic effect, in which light is directly

[a]Department of Materials Science and Engineering, National University of Singapore, 7 Engineering Drive 1, 117574 Singapore, Singapore. E-mail: msewangj@nus.edu.sg
[b]Department of Materials Science and Engineering, University of California, 210 Hearst Mining Building, Berkeley, CA 94720, USA
[c]School of Power Engineering, Chongqing University, 174 Shazhengjie, Shapingba, Chongqing, 400044, China

Zhen Fan received his B.S. degree in Materials Science and Engineering from Shanghai Jiao Tong University in 2007. He is currently a Ph.D. candidate at the National University of Singapore, and also a visiting student researcher at the University of California, Berkeley. His research interests include photovoltaic, ferroelectric, and multiferroic materials and devices.

Dr Kuan Sun is a tenure-track Assistant Professor at the School of Power Engineering in Chongqing University, China. He received B.Appl.Sci. (Hon.) and Ph.D. degrees from the National University of Singapore (NUS), and post-doc trainings at the University of Melbourne and NUS. He was also a visiting scholar at Karlsruhe Institute of Technology and Max-Planck Institute for Polymer Research. His research focuses on printable solar cells, transparent electrodes as well as novel functional materials and devices.

converted into electricity. Commercialized photovoltaic technologies are dominated by silicon solar cells. Despite the continuous effort in reducing their prices, technological development of this silicon-based photovoltaic technology has been slow in recent years. In contrast, aiming to shorten energy payback time[1] and to provide new features, such as mechanical flexibility, light weight and choice of colors, much effort has been devoted to the development of new types of photovoltaic materials, novel cell architectures and advanced operation mechanisms. In the past one decade, a variety of photovoltaic technologies were under intensive research, including dye-sensitized solar cells,[2–6] polymer solar cells,[7–11] molecular solar cells,[12–15] and quantum dot solar cells.[16–19] More recently, a flurry of research interest from the photovoltaic community has concentrated on perovskite materials, including both organic–inorganic halide perovskites[20] and ferroelectric oxide perovskites.[21]

Organic–inorganic halide perovskites have emerged recently as a promising material for the next generation solar cells with both high efficiency and low cost. It was first attempted in 2009 to use halide perovskites $CH_3NH_3PbX_3$ (X = Br and I) as sensitizers in liquid-electrolyte-based dye-sensitized solar cells (DSSCs); however, the power conversion efficiency (PCE) and cell stability were poor due to the corrosion of perovskite by the liquid electrolyte.[22] A key advance was made in 2012 by replacing the liquid electrolyte with a solid hole transporting material (HTM), which resulted in both high PCE of 9.7% and enhanced cell stability.[23] Since then, tremendous enthusiasm and effort have been devoted to the research of halide perovskite-based solar cells. A variety of cell architectures have been developed and the PCEs have been boosted to 20.1% (ref. 24) over the past four years. The efficiency race continues; meanwhile, fundamental studies have revealed the superior optical and electrical properties of halide perovskites, including appropriate bandgap, high absorption coefficient, long and balanced electron–hole diffusion lengths, and large dielectric constant, all of which are desirable properties for photovoltaics. More recently, it was reported that halide perovskite-based photovoltaic devices could show a giant switchable photovoltaic effect due to ion drift, thus endowing halide perovskites with a new potential opto-electronic application in memristors.[25,26]

Photovoltaic effect in ferroelectrics (most of which are ferroelectric oxide perovskites), on the other hand, was discovered in as early as 1950s[27] and is now gaining increasing attention. Early studies[28,29] revealed that steady-state photocurrent could be generated in the homogeneous bulk region of a ferroelectric with inherent non-centrosymmetry, and a photovoltage far beyond the bandgap could be achieved. In this regard, the photovoltaic effect in ferroelectrics is essentially different from photovoltaic effects based on conventional junction structures, such as the p–n junction and Schottky junction, in which the charge separation is realized by the built-in potential near the interface and thus the output photovoltage is limited by the bandgap of the semiconductor absorber. Recently, an alternative and novel mechanism was proposed to explain the above-bandgap photovoltage observed in ferroelectrics, which relied on the nanoscale domain walls for photovoltaic charge generation and separation. Due to the series connection of periodic domain walls (analogous to tandem solar cells), the additive effect of the photovoltage produced in each domain wall can eventually lead to a very large open-circuit voltage. Another fascinating feature of the photovoltaic effect in ferroelectrics is that both signs and magnitudes of photovoltage and photocurrent depend on the ferroelectric polarization, providing a non-destructive way to read out the nonvolatile information stored by the ferroelectric polarization.[30] However, in terms of the photovoltaic efficiency, ferroelectric oxide perovskites cannot yet compete with conventional semiconductors as well as organic–inorganic halide perovskites, due to their limited light absorption (E_g = 3–4 eV) and poor bulk conductivities, which adversely affect the overall performance. The multiferroic oxide perovskite $BiFeO_3$ having a relatively narrow bandgap (2.2–2.7 eV) and robust polarization ($\sim$90 $\mu C\ cm^{-2}$) emerges as a suitable ferroelectric photovoltaic material, and thus has been subjected to extensive study recently.[31–33] More recent progress has demonstrated that PCE as high as 8.1% can be achieved in a double perovskite Bi_2FeCrO_6 through bandgap engineering.[34] This stunning finding, reminiscent of bandgap optimization in organic–inorganic halide perovskites (*e.g.*, from $CH_3NH_3PbI_3$ to $NH_2CH{=}NH_2PbI_3$ (ref. 24)), will inevitably spur the research on bandgap engineering in ferroelectric oxide perovskites for high-efficiency photovoltaics. Also, their potential photovoltaic applications are not restricted to solar cells, but can be extended to opto-electronic memories,[30] photo-actuators,[35] photo-sensors and dosimeters,[36] and even junction devices showing spin-polarized photocurrent,[37] due to the combination of photovoltaic properties with other rich properties, such as ferroelectricity, piezoelectricity, and even multiferroic ordering.

In this paper, we review two recently widely studied photovoltaic materials, both of which belong to perovskites: organic–inorganic halide perovskites and ferroelectric oxide perovskites. The review follows the commonly understood procedure of organization: first we describe the material nature related to the photovoltaic effect, and then discuss the photovoltaic mechanisms. We will highlight their respective merits of structural,

Professor John Wang is Professor and Head of the Department of Materials Science and Engineering, and Senior Faculty Member, NUS Graduate School for Integrative Sciences & Engineering (NGS), NUS. He has more than 30 years of experience in teaching and research of functional materials and materials chemistry. His current research focuses include: functional materials, device materials, nanohybrids for bioimaging and healthcare, and nanostructured materials for sustainable energy. He has published >300 papers in prestigious, top international refereed journals. He has been invited, on a regular basis, to give keynote/invited lectures at major international conferences/symposia/workshops.

optical and electrical properties which are beneficial to the photovoltaic effect, and also point out those weaknesses which need to be improved. The photovoltaic mechanisms are discussed in detail, although some mechanisms still remain controversial. We end this review by raising open questions and future prospects for both perovskites, followed by a brief summary.

2. Organic–inorganic halide perovskites

2.1 Crystal structure

Perovskite compounds have a common chemical formula ABX_3, where the A and B cations occupy the corner and the body-center of the pseudocubic unit cell, respectively, while the X anion resides at the face-center. The perovskite structure can be alternatively viewed as corner-linked BX_6 octahedra with interstitial A cations. In this particular structure, a geometric parameter called the tolerance factor ($t = (R_A + R_X)/\{\sqrt{2}(R_B + R_X)\}$, where R_A, R_B, and R_X are the radii of the corresponding ions) is often used to evaluate the structural formability and stability.[38] Empirically, a perovskite tends to adopt an ideal cubic structure when t is close to 1, while it tends to be distorted into a low-symmetry structure when t is smaller than 1. Note that t is not the only predominant factor to determine the formability and stability of a perovskite structure because other non-geometric factors, such as the bond valence and chemical stability, are also important. As the long-term stability of perovskites is one of the key concerns for outdoor photovoltaic applications, the above knowledge suggests that several aspects need to be considered to improve the stability. Firstly, the constituent elements and groups shall have appropriate sizes to make the perovskite structure geometrically robust. Then, those elements and groups shall be less reactive under ambient conditions (*i.e.* in the presence of moisture and oxygen), and otherwise some protective layers can be incorporated into the photovoltaic devices.

For the organic–inorganic halide perovskites of present interest, the A-sites in the generic ABX_3 formula are universally occupied by organic groups, such as methylammonium ($CH_3NH_3^+$ or MA^+) or formamidinium ($NH_2CH{=}NH_2^+$ or FA^+). The cation B is typically a divalent metal ion (Pb^{2+} or Sn^{2+}), while the anion X is a halide ion (I^-, Br^-, or Cl^-). Because the B cations are essential for the electronic structures of halide perovskites (*vide infra*) and their radii are large, the A-sites shall be occupied by cations with large sizes to satisfy $t \approx 1$. The ingeniousness of the halide perovskite structure therefore lies in that the relatively larger radii of organic groups ($R(MA^+) = 0.18$ nm (ref. 39) and $R(FA^+) = 0.19$–0.22 nm (ref. 40)), compared with those of inorganic ions such as Cs^+ (the largest group-I ion with $R(Cs^+) = 0.167$ nm), can draw t closer to 1 and thus stabilize the perovskite structure. The calculated t of a series of halide perovskites are in the range of 0.8–1 (Fig. 1a), which is a typical feature of perovskites. Note that replacing Pb with Sn seems to increase t; however, the stability becomes poor. This is because, as discussed above, t is not the only predominant factor, and Pb is less vulnerable to oxidization compared with Sn due to the relativistic effects.[41]

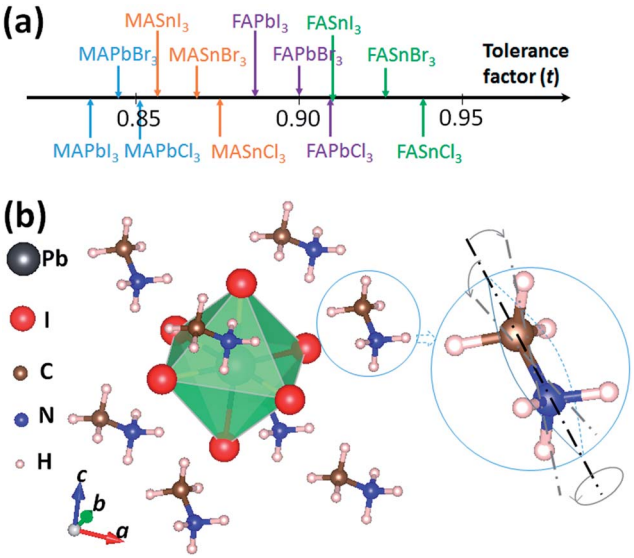

Fig. 1 (a) Tolerance factors (t) of a series of halide perovskites. (b) Crystal structure of $MAPbI_3$ represented by an ABX_3 primitive unit cell. The right panel of (b) shows the orientational disorder of MA^+ molecules.

One interesting aspect is the structural flexibility of organic groups, which makes the crystal structures of halide perovskites versatile. Taking $MAPbI_3$ (Fig. 1b) as an example, as temperature decreases, the disorder–order transition of MA^+ groups triggers the phase transition of $MAPbI_3$.[42–45] When the temperature is above ~372 K, the MA^+ groups are randomly oriented so that the cubic *Pm*3*m* symmetry (α phase) is preserved. In the temperature range of 162–372 K, the MA^+ groups become less disordered, which leads to a tetragonal *I*4/*mcm* symmetry (β phase). When the temperature is below ~162 K, the MA^+ groups are frozen and the symmetry of $MAPbI_3$ is further lowered to become orthorhombic (γ phase); however, whether a non-centrosymmetric space group ($Pna2_1$ (ref. 42)) or a centrosymmetric one (*Pnma*[45]) should be assigned to the γ phase is controversial. The diagnostic modes corresponding to the orientational disorder of MA^+ groups in α and β phases have been specifically studied by both Raman and infrared (IR) spectroscopies.[46–48] It should be pointed out that such an orientational disorder of MA^+ groups makes it impossible to simulate α and β phases precisely by the density functional theory (DFT) which is based on 3-D periodic boundary conditions.[49] Fortunately, previous theoretical studies have reported that the basic electronic structures of $MAPbI_3$ do not depend sensitively on the orientations of MA^+ groups.[49,50]

2.2 Electronic structure

From Kubelka–Munk transformed diffuse reflectance spectra and ultraviolet photoelectron spectra (UPS), the bandgap, VBM and CBM of $MAPbI_3$ were estimated to be 1.5, −5.43, −3.93 eV, respectively.[23,45] The bandgap was later determined to be 1.61 eV for $MAPbI_3$ grown on mesoporous TiO_2, by using optical approaches including diffuse reflectance spectra, photoconductance, photoluminescence and transient absorption

spectroscopy.[51] More recently, the electronic structures of $MAPbI_3$ and its interface energetics in solar cells were fully investigated by UPS and inverse photoemission spectroscopy (IPES). The electronic bandgap of $MAPbI_3$ was measured to be 1.7 eV,[52] which was larger than the typical values measured optically.

The electronic structures of halide perovskites have also been investigated by DFT calculations. Despite the limitations mentioned above, DFT calculations have yielded results in substantial agreement with experimental measurements and therefore can shed light on the origins of the excellent photovoltaic properties of halide perovskites. Initial calculations for the electronic structures of $MAPbI_3$,[45,53] using DFT without taking into account the spin–orbit coupling (SOC) effects, revealed bandgaps which were in good agreement with the experimental values (~1.5 eV).[23,45] However, this fortuitous agreement was later explained to be caused by the error cancellations between neglecting SOC and the bandgap underestimation error in the DFT generalized gradient approximation (GGA).[54,55] It is therefore of importance to employ computational methods allowing for the complex effects such as SOC, many-body effects and van der Waals interactions in the lead-based organic–inorganic hybrid systems, to appropriately calculate the electronic structures. So far many computational methods have been used, for example, PBE + SOC,[56,57] HSE + SOC,[58] and GW + SOC.[41,59,60]

Yin *et al.*[50,61] investigated the electronic structure of the $MAPbI_3$ cubic phase by using DFT-GGA and obtained plausible results which could account for the superior optical and electrical properties of $MAPbI_3$ (results of tetragonal and orthorhombic phases are not shown here and can be found elsewhere[45,61]). The calculated results of the band structure, density of states (DOSs), and partial charge densities at the valence band maximum (VBM) and conduction band minimum (CBM) are shown in Fig. 2. The band structure of $MAPbI_3$, as shown in Fig. 2a, exhibits a direct bandgap of 1.5 eV at the *R* point. By comparing the total and partial DOSs (Fig. 2b–e), one can see that the CBM is dominated by the Pb p orbital, whereas the VBM is constituted by I p states mixed with a small amount of Pb s states. The optical transition of $MAPbI_3$ thus relies on a direct bandgap p–p transition, leading to strong optical absorption coefficients.[61] The partial charge densities (Fig. 2f and g) further reveal the ionic feature of CBM and strong antibonding coupling between Pb s and I p at VBM. The strong p–s antibonding enhances the dispersion of the upper valence bands. The well-dispersed bands near both CBM and VBM (Fig. 2a) therefore result in small effective masses of both electrons (m_e^*) and holes (m_h^*). The m_e^* and m_h^* are calculated to be $0.35m_0$ and $0.31m_0$ respectively without considering SOC, and are reduced to $0.18m_0$ and $0.21m_0$ respectively considering SOC.[61,62] Such small m_e^* and m_h^* are responsible for the experimentally observed good ambipolar electrical conductivity.[63] Further theoretical studies showed that m_e^* and m_h^* are anisotropic, stemming from rotations of the PbI_6 octahedra.[64,65] In addition, Fig. 2c also reveals that the states of MA^+ cations are located far from band edges (CBM and VBM), suggesting that the role of MA^+ cations, in terms of electronic properties, is just to maintain overall charge neutrality.[50,65,66] More recent studies

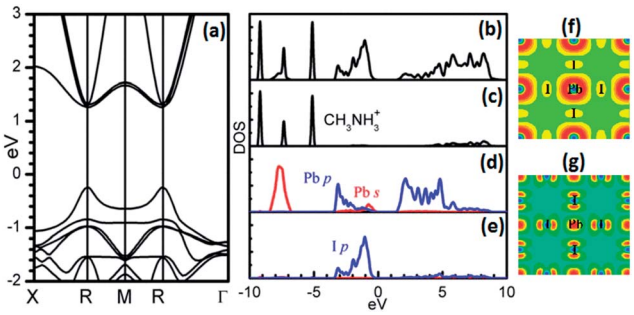

Fig. 2 (a) Band structure; (b) total DOS; partial DOSs of (c) MA^+, (d) Pb, and (e) I; partial charge densities at (f) CBM and (g) VBM of $MAPbI_3$. Reproduced from ref. 50, Copyright 2014, AIP Publishing LLC.

reported the indirect impact of the MA^+ cations on the shape and the orbital composition of the band edges.[60,67] This indirect impact was interpreted as that the interaction between MA^+ cations and $[PbI_3]^-$ networks affects the cell size and thus the bonding of Pb–I, which gives rise to the modulation of density of states near band edges.

Besides $MAPbI_3$ as reviewed above, other halide perovskites (ABX_3) possess similar construction ways of electronic bands, *i.e.*, the VBM has strong B s and X p antibonding character and the CBM mainly contains B p states.[57] However, detailed band parameters, such as the bandgap and the energy positions of VBM and CBM, can differ with the variation of elements in ABX_3 perovskites. This indicates that element substitution may be effective to further optimize the perovskite materials as light absorbers (note that the bandgap of $MAPbI_3$ is 1.5–1.6 eV, slightly larger than the ideal value of 1.34 eV as predicted by the Shockley–Queissier limit[68]). For example, Amat *et al.*[60] predicted that replacing an A-site cation of MA with FA could induce a slight bandgap reduction (~0.2 eV when SOC + GW was used) in Pb-based perovskites, which was due to the modulation of the Pb–I bond character stemming from the interplay of size effects and enhanced hydrogen bonding between the FA cations and the inorganic networks. Koh *et al.*[69] provided experimental evidence for the bandgap reduction in $FAPbI_3$ ($E_g = 1.47$ eV) by measuring UV-vis absorption spectra. The B-site substitution of toxic Pb by environmentally friendly Sn is promising, because $MASnI_3$ exhibits a smaller bandgap (1.1 eV in theory[41] and 1.2–1.35 eV obtained from optical diffuse reflectance measurements[44]) and reduced effective mass of holes.[41] However, Sn has poor stability against oxidation, which turns Sn-based perovskites into p-type Sn^{4+}-doped semiconductors with metal-like conductivity.[44,70] As the halide ion X in $MAPbX_3$ varies from I to Br to Cl, the lattice constant decreases and the bandgap increases from 1.57 to 1.80 to 2.34 eV in theory[54] (1.53 → 2.20 → 3.00 eV from optical diffuse reflectance data[71]). The calculated bandgaps follow the experimental trend qualitatively, while there is also a sizable underestimation of bandgaps (especially for X = Cl) caused by the calculation method of GGA-DFT. In regard to the origin of the electronic structures changing with halide ions, Lindblad *et al.*[72] suggested that the intrinsic differences in energy levels of halide ions rather than the different lattice parameters played a major role. In addition,

mixed halide $MAPbI_{3-x}X_x$ (X = Br, Cl) perovskites were also investigated, and it was found that Br-doping increased the bandgap significantly[54,73] while Cl-doping led to an almost unchanged bandgap and optical absorption onset.[54,74] The reason behind the minor effect of Cl-doping on the electronic and optical properties of mixed halide perovskites might be due to that the amount of the dopant Cl was negligible in the final products of perovskite thin films, as evidenced by X-ray photoelectron spectroscopy (XPS)[75] and scanning transmission electron microscopy-energy dispersive spectroscopy (STEM-EDS).[76] However, we also note that preparation methods and conditions, such as the annealing temperature and environment, can make a significant difference in terms of perovskite film compositions.[77,78] This might be related to the lower sublimation temperature of methylammonium chloride (MACl) than that of MAI, PbI_2, or $PbCl_2$.[79]

2.3 Optical properties

Thanks to the near-ideal bandgap (1.5–1.6 eV) and the direct bandgap p–p transition as discussed above, $MAPbI_3$ exhibits a wide absorption spectrum up to a wavelength of 800 nm, and a large optical absorption coefficient (10^4 to 10^5 cm^{-1} in the wavelength range smaller than 600 nm).[80–82] The optical absorption coefficient of $MAPbI_3$ is higher than or at least comparable to that of conventional semiconductors, such as GaAs, CdTe, Cu(In,Ga)Se_2 (CIGS), evidenced by both first-principles calculation[61] and optical absorption measurements.[83] Such a large absorption coefficient over a broad wavelength range thus endows $MAPbI_3$ with the advantage of absorbing incident light efficiently while keeping the absorber layer thickness small. Because optical absorption is undoubtedly crucial for the photovoltaic performance, it is tempting to further extend the absorption to longer wavelengths and/or to improve the absorption coefficient. As mentioned above, the element substitution in ABX_3 perovskites is a powerful tool to engineer the band structure and thus impact the optical properties. One example is $FAPbI_3$, which shows a more favorable bandgap (1.47 eV) compared with $MAPbI_3$ and therefore allows light absorption beyond 800 nm. It should be highlighted that $FAPbI_3$ based solar cells were demonstrated very recently to exhibit a certified PCE as high as 20.1%.[24] Another two examples of $MASn_{1-x}Pb_xI_3$ (ref. 84) and $MAPb(I_{1-x}Br_x)_3$ (ref. 85) are also presented here. Fig. 3a shows that the intermediate solid solutions of $MASn_{1-x}Pb_xI_3$ with $x = 0.25$ and 0.5 exhibit the smallest bandgap of 1.17 eV. In the other mixed perovskite of $MAPb(I_{1-x}Br_x)_3$, as shown in Fig. 3b, a systematic blue shift of the absorption onset with increasing Br content is observed.

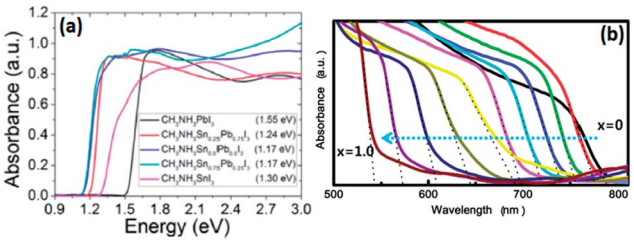

Fig. 3 UV-vis absorption spectra of (a) $MASn_{1-x}Pb_xI_3$ (reproduced from ref. 84, Copyright 2014, ACS) and (b) $MAPb(I_{1-x}Br_x)_3$ (reproduced from ref. 85, Copyright 2013, ACS).

2.4 Electrical properties

2.4.1 Charge transport properties. Good ambipolar electron and hole transport properties in organic–inorganic halide perovskites have been reflected by the experimental facts that remarkable photovoltaic efficiencies could be achieved in a variety of solar cell architectures. For example, a meso-superstructured perovskite solar cell with a high efficiency of 10.9% was developed by replacing the TiO_2 photoanode with an insulating Al_2O_3 scaffold which does not assist in the electron extraction,[86] implying that the perovskite itself is a good electron transporter. In addition, a satisfactory efficiency of 5.5% was demonstrated in a perovskite solar cell with a HTM-free configuration,[87] indicating that the perovskite also efficiently conducts holes. More unexpectedly, high photovoltaic efficiencies were achieved in perovskite solar cells with thin-film planar heterojunction structures.[88,89] All of the above experimental findings suggest that the organic–inorganic halide perovskites are capable of transporting electrons and holes simultaneously and efficiently. The ambipolar charge transport properties of halide perovskites can be attributed to the small and balanced electron and hole effective masses (see the calculated results in Section 2.2), and can be further evidenced by the measurement of large carrier mobility. Wehrenfennig *et al.*[90] derived carrier mobility of ~8 $cm^2\ V^{-1}\ s^{-1}$ and 11.6 $cm^2\ V^{-1}\ s^{-1}$ for $MAPbI_3$ and $MAPbI_{3-x}Cl_x$, respectively, from THz photoconductivity onset values. Ponseca *et al.*[91] reported even larger carrier mobility of 25 $cm^2\ V^{-1}\ s^{-1}$ for $MAPbI_3$, through comparing THz photoconductivity kinetics and optical transient absorption kinetics. Wang *et al.*,[92] using Hall effect measurement, obtained carrier mobility of 3.9 $cm^2\ V^{-1}\ s^{-1}$ for $MAPbI_3$ with a stoichiometric precursor ratio (1 : 1) and also found that the carrier mobility was a function of MAI/PbI_2 precursor ratio. The charge carrier mobility can be effectively tuned by, *e.g.*, replacing Pb by Sn[44] and forming a mixed halide perovskite.[90]

2.4.2 Dielectric properties. The dielectric constant (also called the relative permittivity) is a complex number given by: $\varepsilon = \varepsilon' - i\varepsilon''$, where the real part ε' represents the charge storage ability and the imaginary part ε'' represents the energy loss. In general, there are four mechanisms of polarization operating in a dielectric material: electronic polarization (P_{ele}), ionic polarization (P_{ion}), dipolar polarization (P_{dp}), and space charge polarization (P_{sc}). These four polarization mechanisms P_{ele}, P_{ion}, P_{dp}, and P_{sc} occur in sequence as the frequency of the applied field decreases, resulting in frequency-dependent dielectric constants. Fig. 4a shows the frequency-dependent ε' of $MAPbI_3$ measured in the dark at room temperature. At optical (ultrahigh) frequencies, only P_{ele} takes part in the dielectric process and therefore a small ε' is obtained (ε'_{opt} = ~6.5 in experiment,[93] while 5.6–6.5 in calculation[66]). As frequency decreases, P_{ion} is involved and a new plateau is reached with ε'_{high} = ~30 (measured at 90 GHz).[42] Further decreasing the frequency can induce the polarization contributed from MA^+ dipoles (P_{dp}), leading to an enhanced ε'

(ε'_{low} = ~60 measured at 100 kHz (ref. 94)). The anomalously large ε' is observed at near-static (ultralow) frequencies (ε'_{sta} > 1000 measured in ref. 95), which is mainly contributed by P_{sc}. Because P_{sc} is caused by excessive charge carriers, such a giant P_{sc} induced ε'_{sta} can provide evidence that there are abundant charge carriers residing in $MAPbI_3$. Under illumination, much more charge carriers are generated and therefore ε'_{sta} can be dramatically enhanced to 10^6 to 10^7 (Fig. 4b).[95] Compared with most organic photovoltaic materials (ε' = 2–4 (ref. 96)) and some inorganic semiconductors (ε' = 9–13 (ref. 97)), halide perovskites exhibit rather large low-frequency dielectric constant (ε' = ~60, and for comparison, only the contributions from P_{ele}, P_{ion}, and P_{dp} are included). The large dielectric constant facilitates the screening effect of Coulombic attraction between photoexcited electron–hole pairs, also known as excitons, so that they can be separated more easily.

2.4.3 Ferroelectricity. In recent studies of organic–inorganic halide perovskites, ferroelectricity has been a frequently quoted property to account for the origin of the excellent photovoltaic performance,[98,99] because charge separation and transport within the ferroelectric domain walls can be very efficient. Ferroelectricity may also be an origin of the hysteresis observed in current–voltage (*I–V*) curves.[100,101] However, although commonly present in inorganic oxide perovskites, ferroelectricity has not been unambiguously demonstrated in halide perovskites so far.

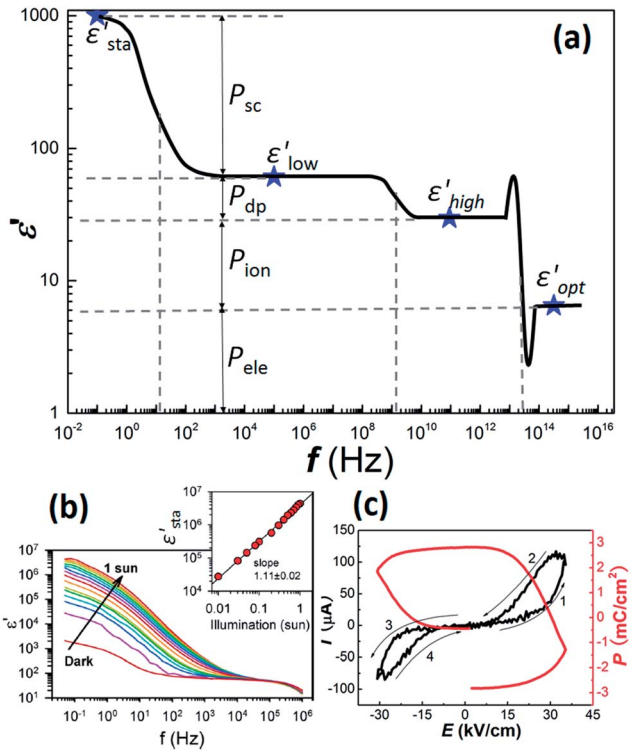

Fig. 4 (a) Frequency-dependent ε' of $MAPbI_3$ in a wide frequency range. Data are collected from ref. 42 and 93–95. (b) ε' of $MAPbI_{3-x}Cl_x$ as a function of frequency measured with various illumination intensities. The inset shows the linear relationship between ε'_{sta} and illumination intensity. Reproduced from ref. 95, Copyright 2014, ACS. (c) *I–E* and *P–E* hysteresis loops of $MAPbI_3$. Reproduced from ref. 102, Copyright 2015, ACS.

β-$MAPbI_3$ was intuitively classified as a ferroelectric phase due to the coexistence of MA^+ permanent dipoles and the distortion of PbI_6 octahedra.[44] This hypothesis was not well justified although some polarization–electric field (*P–E*) hysteresis loops were provided as evidence.[44,101] The *P–E* loops were later shown to be simply caused by leakage current, because in the corresponding *I–E* curves, the current peaks located in the vicinity of coercive fields, which are typical ferroelectric characteristics, were however absent (Fig. 4c).[102] Kutes *et al.*[103] claimed that ferroelectric domains of $MAPbI_3$ were directly observed *via* piezoresponse force microscopy (PFM), while Xiao *et al.*[104] and Fan *et al.*[102] reported that there was no observation of domain-like structures and the previous finding might be associated with some artifacts in PFM. Conflicting results were also found in DFT calculations. Zheng *et al.*[105] found that the most stable structure of β-$MAPbI_3$ is antiferroelectric with zero polarization, while Frost *et al.*[98] and Fan *et al.*[102] predicted ferroelectric structures for β-$MAPbI_3$ with however significantly different polarization values. In a comprehensive study conducted by Fan *et al.*,[102] it was suggested that $MAPbI_3$ was not ferroelectric at room temperature, because the dynamic orientational disorder of MA^+ dipoles and the large leakage current would disfavour the formation and the switching of ferroelectric domains, respectively. Despite the above controversies, it is of great interest to conduct further studies of ferroelectricity in halide perovskites especially at low temperature, in which case the disorder–order transition would occur and the leakage current would be reduced.

2.5 Device architectures

A variety of device architectures of halide perovskite-based solar cells have been developed so far. Their structural evolution is depicted in Fig. 5. Derived from DSSCs, the initial halide perovskite-based solar cell adopted nanodot perovskite as a sensitizer (Fig. 5a).[23] In this configuration, the concentration of the deposited perovskite was low and therefore the light absorption efficiency was poor. In the meso-superstructured perovskite solar cell (Fig. 5b),[86] the mesoporous TiO_2 was replaced with insulating Al_2O_3, and a thin and continuous perovskite film was coated on the surface of Al_2O_3. Electron transport was therefore realized within the perovskite layer and the efficiency was slightly improved due to the good electron conductivity of the perovskite. As the amount of perovskite increased, the pores of the mesoporous metal oxide became filled and an excessive capping layer of perovskite was formed (Fig. 5c). In this case, both one-step and two-step[107] procedures could be applied for coating the perovskite, while the latter procedure could result in better uniformity of perovskite precipitation and therefore higher efficiency. Milestones were achieved by developing planar heterojunction solar cells (Fig. 5d), in which the device architecture was simplified and surprisingly even higher efficiency was achieved.[89] This particular configuration of solar cell took full advantage of the ambipolar electron and hole transport properties of halide perovskites.

2.6 Photovoltaic mechanisms

2.6.1 Charge generation, separation and diffusion. Upon illumination, the absorption of photons by halide perovskites

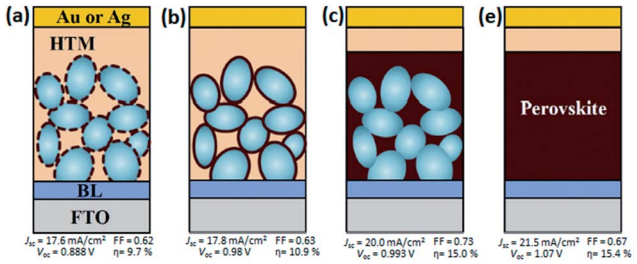

Fig. 5 Structural evolution of halide perovskite-based solar cells: (a) sensitized solar cell with nanodot perovskite, (b) meso-superstructured solar cell with a thin and continuous layer of perovskite, (c) perovskite-infiltrated solar cell with a capping layer of perovskite, and (d) planar heterojunction solar cell. Reproduced from ref. 106, copyright 2014, Elsevier. Typical photovoltaic parameters of each solar cell in (a), (b), (c), and (d) are cited from ref. 23, 86, 107 and 89, respectively.

generates electron–hole pairs (*i.e.* excitons) within a few picoseconds.[108] These excitons have binding energies ranging from 19 to 50 meV,[109] which are sufficiently low and comparable to the thermal energy at room temperature ($k_BT \sim 25$ meV). Therefore, after thermalization, the initial excitons evolve into either highly delocalized Wannier-type excitons or free charge carriers. Here, the large dielectric constant of halide perovskites facilitates the dissociation of excitons. These two photoexcited species may coexist in the subsequent diffusion process.

The diffusion length of a charge carrier is determined by its mobility and lifetime. On the one hand, as has already been described in Section 2.4.1, the charge carrier mobility in halide perovskites is large. On the other hand, the charge carrier lifetime in halide perovskites is extremely long because of the exceptionally low recombination rate. Using transient THz spectroscopy and time-resolved photoluminescence spectroscopy, Wehrenfennig *et al.*[90] showed that the monomolecular recombination (first order; including geminate recombination and/or trap-assisted recombination) rates were $\sim 5\ \mu s^{-1}$ for $MAPbI_{3-x}Cl_x$ and $\sim 15\ \mu s^{-1}$ for $MAPbI_3$, the bi-molecular recombination (second order) rates were at least four orders of magnitude lower than the Langevin limit, and the Auger recombination (third order; involving three particles and the recombination energy is transferred to a third electron) was insignificant when the excitation intensities were low (note that the ambient sunlight excitation was low-intensity exication). Similarly, Ponseca *et al.*,[91] using the technique of time-resolved microwave conductivity, reported that at the low excitation intensity, the timescale of geminate and nongeminate recombination as well as charge carrier relaxation was larger than 1 μs.

Theoretical calculations have been used to unravel the suppressed trap-assisted recombination in halide perovskites. Various types of defects and their associated trap states in the band structures have been investigated. Schottky defects, such as PbI_2 and MAI vacancies, were found not to create trap states within the bandgap.[110] Elementary defects derived from Frenkel defects, such as MA, Pb and I vacancies, formed shallow levels near the band edges acting as unintentional doping sources.[110] Anti-site substitutions and Pb interstitials could create deep levels (note that deep-level traps are responsible for the non-radiative recombination); however, their high formation energies indicated that they were difficult to form.[50] Therefore, it has been theoretically suggested that the trap-assisted recombination rates in halide perovskites shall be slow.

With the interpretation of the above experimental and theoretical results, one would expect the electron–hole diffusion lengths of halide perovskites to be long. There have been a couple of studies demonstrating the long and balanced electron–hole diffusion lengths, by using photoluminescence (PL)-quenching measurement,[63,81] transient absorption spectroscopy,[81] photocurrent/photovoltage spectroscopy,[111] impedance spectroscopy,[112] and electron beam-induced current measurement.[113] Here we show one example of PL-quenching measurement conducted by Stranks *et al.*[63] As shown in Fig. 6, the addition of an electron- or hole-quenching layer (PCBM or Spiro-OMeTAD, respectively) onto the perovskite film accelerates the PL decay, which is more noticeable in $MAPbI_{3-x}Cl_x$ compared with $MAPbI_3$. In addition, as can be seen from the inset of Fig. 6a, the time constant of the PL decay of $MAPbI_{3-x}Cl_x$ with PMMA is 272.7 ns, while that of $MAPbI_3$ is only 9.6 ns. By modelling the PL decay dynamics according to the one-dimensional diffusion equation, the diffusion lengths of both electrons and holes in $MAPbI_3$ were estimated to be ~100 nm, while much longer electron–hole diffusion lengths of $MAPbI_{3-x}Cl_x$ were extracted (~1 μm). This finding could well explain that the optimum thickness of the perovskite layer for the highest efficiency in the planar heterojunction solar cell was only ~140 nm for $MAPbI_3$, while it was much larger (~500 nm) for $MAPbI_{3-x}Cl_x$. A later report[114] showed that a planar heterojunction solar cell based on the ~350 nm-thick $MAPbI_3$ film prepared by a vapor-assisted solution process achieved high efficiency of 12.1%, suggesting that the electron–hole diffusion lengths in high-quality $MAPbI_3$ could exceed previously reported values.

2.6.2 Charge extraction. Efficient charge extraction, *i.e.* transferring electrons and holes from the absorber to their respective conducting channels (ETM and HTM) or directly to electrodes, is crucial for the solar cell performance. The charge extraction mechanism may vary depending on the specific solar cell architecture. Investigations into those mechanisms are therefore of great importance for both fundamental understanding and further device optimization.

The working mechanisms in perovskite sensitized solar cells (Fig. 5a) are similar to those in DSSCs, in which photoexcited electrons (holes) are immediately injected from the perovskite into ETM (HTM) while the charge transport occurring in the perovskite can be negligible.

In the perovskite/mesoporous TiO_2 solar cell (Fig. 5b and c), the exact electron extraction mechanism has not been well established. Because the perovskite itself has good electron conductivity, there may be two pathways of electron extraction in this particular cell architecture: (i) electron injection from the perovskite to TiO_2, and (ii) electron transport within the perovskite itself. The controversies thus arise as to which pathway does exist and which pathway is more efficient if both of them coexist. Using transient photocurrent decay measurement, Lee *et al.*[86] found that replacing mesoporous TiO_2 by

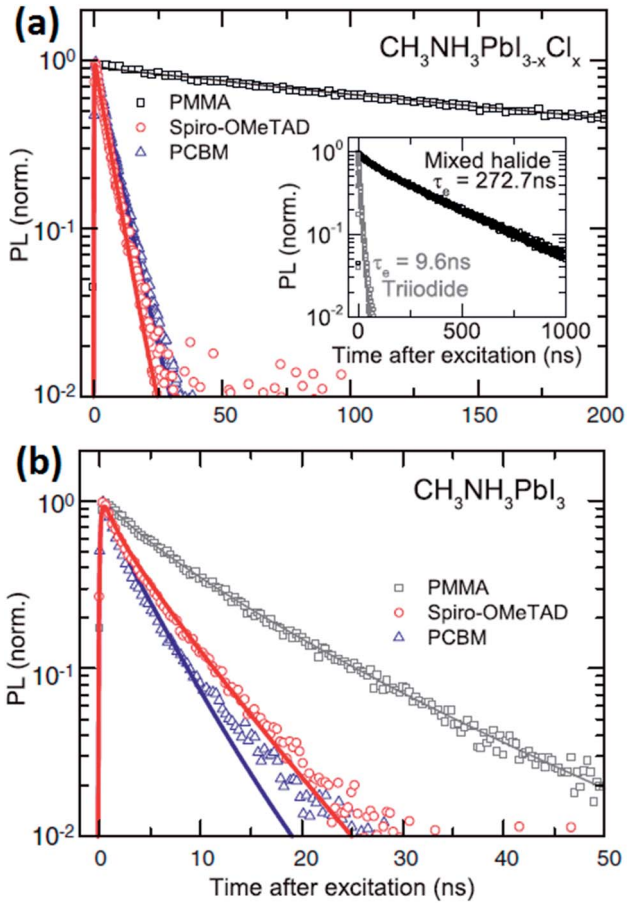

Fig. 6 Time-resolved PL measurements of (a) $MAPbI_{3-x}Cl_x$ and (b) $MAPbI_3$ with PCBM (electron quencher), Spiro-OMeTAD (hole quencher) and PMMA top layers, respectively. The inset in (a) shows the comparison of PL decays of the two perovskites with the PMMA top layer. Reproduced from ref. 63, Copyright 2013, Science (AAAS).

insulating Al_2O_3 could result in faster charge collection, indicating that the electrons were more efficiently transported through the perovskite layer rather than TiO_2. In contrast, by employing femtosecond transient absorption spectroscopy, Marchioro *et al.*[115] provided clear evidence for efficient electron injection from $MAPbI_3$ to TiO_2 with ultrafast femtosecond-to-picosecond timescales and the charge recombination was significantly slower when TiO_2 rather than Al_2O_3 was used. The efficient electron injection from $MAPbI_3$ to TiO_2 was also confirmed by Ponseca *et al.*[91] through studying the transient THz photoconductivity kinetics. In addition, they also revealed that the charge transport was unbalanced due to the low intrinsic electron mobility of TiO_2, and therefore proposed that using a metal oxide with higher electron mobility may further enhance the performance of the perovskite/mesoporous metal oxide solar cells.

The charge extraction mechanism of planar heterojunction solar cell (Fig. 5d) was well elucidated by Edri *et al.*,[113] by performing a direct measurement of electron beam-induced current (EBIC) profiles of the cross-sections of a $MAPbI_{3-x}Cl_x$-based planar solar cell (Fig. 7a). In this technique, the EBIC signal is a current formed by collecting charge carriers generated by the electron beam. The EBIC image is therefore a map showing where in the cell the charge carriers are generated, and the relative EBIC peak intensities further indicate the extraction efficiency of charge carriers. A cross-sectional secondary electron (SE) image and the corresponding EBIC image are shown in Fig. 7b. Fig. 7c presents the line profiles of SE and EBIC taken at the region as indicated in Fig. 7b. The EBIC line profile displays a pronounced two-peak pattern, indicating the coexistence of hole and electron extractions. The electron extraction has higher efficiency because the peak near the HTM is higher than that close to the TiO_2. In addition, the dip between two peaks is an indicator of the recombination of charge carriers during diffusion. These results demonstrate that the $MAPbI_{3-x}Cl_x$ planar configured solar cell works as a p–i–n heterojunction. In the p–i–n heterojunction, two built-in fields, which are formed as a result of the energy band alignments at two interfaces of HTM/$MAPbI_{3-x}Cl_x$ and $MAPbI_{3-x}Cl_x$/compact TiO_2 (Fig. 7d), are responsible for hole and electron extractions, respectively. Note that the observation of a two-peak pattern in the EBIC line profile is achievable only when the absorber thickness exceeds the diffusion lengths. As the absorber thickness decreases, there is a transition of the EBIC peak from a double peak to a single peak, which is due to the superposition of the two junction regions in the p–i–n model. According to the EBIC line profiles, the diffusion lengths of electrons and holes are calculated as ~1.9 μm and ~1.5 μm, respectively, which were consistent with those reported by Stranks *et al.*[63] On the other hand, using the same EBIC technique, Edri *et al.*[113] also studied the device without HTM, in which case only a single peak was observed, suggesting the formation of a p–n junction between $MAPbI_{3-x}Cl_x$ and TiO_2. Aharon *et al.*[116] further revealed that the photovoltaic performance of the HTM-free perovskite solar cell was dependent on the depletion width of the perovskite/TiO_2 junction.

Recent studies demonstrated that the p–i–n or p–n structure could be reversibly changed due to the ion drift induced modulation of the band alignments near the interfaces.[25,26] The mobile ions were proposed to be vacancies of MA, Pb and I.[25] Here an ITO/PEDOT:PSS/$MAPbI_3$/MoO_3/Al thin film planar heterojunction[26] is taken as an example. As deduced from the ideal energy-level diagram (Fig. 8a), the heterojunction in the virgin state (no interface charge) acts as a hole conductor (Fig. 8b). When a positive poling voltage is applied to an Al electrode, the positive (negative) ions drift toward ITO/PEDOT:PSS (MoO_3/Al) and accumulate near the interface, which causes significant band bending (Fig. 8c). In this case, a diode with the forward direction from Al to ITO is formed. The similar working principle is applicable to the negative poling process (Fig. 8d), and in this case the diode forward direction is reversed. Therefore, the switching of the p–i–n structure is realized, and consequently switchable photocurrents are observed (Fig. 8e). This switching behaviour of the photovoltaic effect was also reported in photovoltaic devices based on ferroelectric oxide thin films, although different origins were found. It should be highlighted that the observed switchable photovoltaic effect may promise the realization of electrically

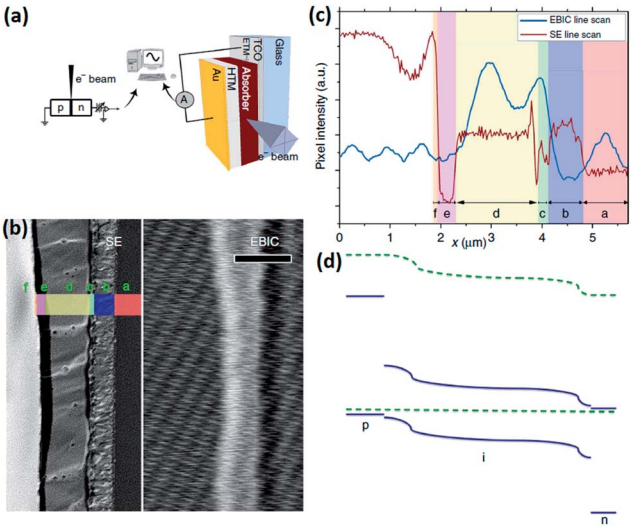

Fig. 7 (a) Schematic set-up of an EBIC experiment on a cross-section of a $MAPbI_{3-x}Cl_x$ planar heterojunction solar cell. (b) SE (left) and corresponding EBIC (right) images. Letters in the SE image denote the layers of: (a), glass; (b), FTO; (c), TiO_2; (d), $MAPbI_{3-x}Cl_x$; (e), HTM; (f), Au. (c) SE and EBIC line profiles at the indicated region in (b), and letters in (c) correspond to those in (b). (d) Schematic energy band diagram of the $MAPbI_{3-x}Cl_x$-based solar cell. Reproduced from ref. 113, Copyright 2014, Nature Publishing Group.

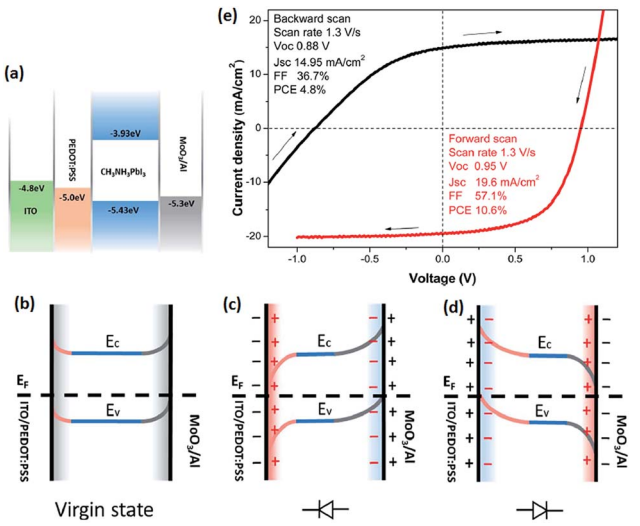

Fig. 8 (a) Ideal energy-level diagram of the ITO/PEDOT:PSS/$MAPbI_3$/MoO_3/Al heterojunction. Schematic energy band alignments of the device in (b) the virgin state, (c) positively poled state (positive voltage is applied to Al), and (d) negatively poled state (positive voltage is applied to Al). Interface charge and screen charge are represented by red and black signs, respectively. Reproduced from ref. 26, Copyright 2015, RSC.

and optically readable memristors based on organic–inorganic halide perovskites.

3. Ferroelectric oxide perovskites

Oxide perovskites always stand at the forefront of condensed matter science as they display a wide spectrum of interesting functional properties, such as catalytic, superconducting, dielectric, piezoelectric, pyroelectric, ferroelectric, ferromagnetic, and multiferroic properties. The broad diversity of the properties of oxide perovskites is associated with their versatile crystal structures, in which around 90% of the metallic natural elements in the periodic table can be accommodated.[117] Among the numerous subclasses of oxide perovskites, ferroelectric oxide perovskites are probably the most promising candidates for the photovoltaic effect, because the inversion symmetry breaking promotes the desirable separation of photoexcited charge carriers. Most studies of the photovoltaic effect in ferroelectrics to date have focused on several typical families of oxide perovskites, such as $LiNbO_3$ (LNO),[28,29,118–121] $BaTiO_3$ (BTO),[122–124] $Pb(Zr,Ti)O_3$ (PZT),[125–128] and $BiFeO_3$ (BFO).[31–34,129–131] These oxide perovskites will therefore be the main focus in the following sections, including their crystal structures and correlation with ferroelectricity, physical properties related to the photovoltaic effect, and photovoltaic mechanisms.

3.1 Crystal structure and correlation with ferroelectricity

In oxide perovskites with the formula of ABO_3, the A cations can be alkali, alkaline earth, rare earth and some large ions such as Pb^{2+} and Bi^{3+}, while the B cations can be 3d, 4d and 5d transition metal ions. The lattice constants of ABO_3 primitive pseudocubic cells are typically ~4.0 Å, which are significantly smaller than those of halide perovskites (~6.2 Å) having large organic cations at the A-site. The ferroelectric phase of an oxide perovskite is formed through the phase transition from the centrosymmetric cubic phase at high temperature to the low-symmetry ferroelectric phase at low temperature, where the paraelectric–ferroelectric phase transition temperature is defined as the Curie temperature (T_c). The symmetry of a ferroelectric phase can only belong to ten polar point groups. Accompanied by symmetry lowering, cations are displaced relative to anions, inducing the electric dipole moment and thus being the origin of spontaneous polarization (P_s). Both A and B cations can undergo ferroelectric displacement, with however different mechanisms. For example, the hybridization of B cation d states (Ti 3d and Nb 4d) and O 2p states is energetically favourable for the off-centre motion of the B cation. On the other hand, the displacement of the A cation is generally driven by the stereochemically active lone pairs (Bi 6s and Pb 6s). To better understand the correlation between structural distortion and ferroelectricity in oxide perovskites, we give an example of BTO. As shown in Fig. 9, BTO undergoes the phase transition from centrosymmetric cubic to tetragonal, orthorhombic, and finally rhombohedral as temperature decreases. The latter three phases tetragonal, orthorhombic and rhombohedral are ferroelectric, and their structures can be viewed as distortions of the cubic structure along its edge, face diagonal and body diagonal, respectively. The Ti displacements and the resulting spontaneous polarizations in those three phases are along [001], [101] and [111] directions, respectively.

The crystal structures of ferroelectric oxide perovskites are also sensitive to chemical composition and strain, besides temperature. For example, in the PZT solid solutions, the

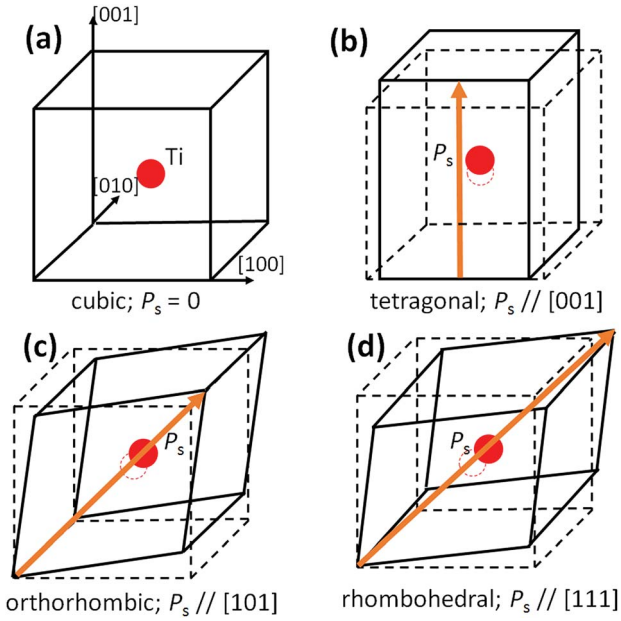

Fig. 9 Schematics showing the structural distortion and the Ti displacement in four $BaTiO_3$ phases (a) cubic (reference), (b) tetragonal, (c) orthorhombic, and (d) rhombohedral. The spontaneous polarization orientations are indicated by brown arrows.

ferroelectric phases can be separated into two by a morphotropic phase boundary (MPB; near Zr/Ti = 52/48): the Ti-rich tetragonal phase ($1 < c/a < 1.06$) and the Zr-rich rhombohedral phase.[132] In BFO thin films, large compressive strain (−4.5%) can induce the phase transition of BFO from rhombohedral-like to tetragonal-like (c/a ~1.25).[133] Because the crystal structure is intimately correlated with the ferroelectric polarization, tuning the chemical composition and strain is an effective way to modify the ferroelectric properties of oxide perovskites.

3.2 Physical properties related to the photovoltaic effect

3.2.1 Dielectric behaviour and ferroelectricity. Large dielectric constants and polarization magnitudes are the innate advantages of ferroelectric oxide perovskites for the separation of photoexcited charge carriers. The dielectric constants are typically 10^2 to 10^3 and can reach 5×10^3 in some PZT-based relaxor perovskites.[134] The spontaneous polarization values of bulk LNO, BTO, PZT, and BFO are ~70, ~25, 10–45, and ~90 μC cm^{-2}, respectively.[135–138] With the advances in thin-film fabrication technologies, the spontaneous polarization values of high-quality epitaxially strained thin films of BTO, PZT, and BFO can be further enhanced to ~70 (c/a = 1.03), ~100 (c/a = 1.06), and ~150 (c/a = 1.25) μC cm^{-2}, respectively.[139–142] Large spontaneous polarization will benefit the photovoltaic charge separation, which may be one of the reasons why the lanthanum-doped PZT (PLZT) epitaxial film (larger P_s due to strain induced structural distortion) showed better photovoltaic performance than its polycrystalline counterpart after poling both films with similar voltages.[143] Note that in the real case, a ferroelectric material will not always exhibit spontaneous polarization macroscopically because of the presence of ferroelectric domains. The actual polarization state of the ferroelectric material is dependent on the magnitude of the poling voltage, which determines the number of switched domains. Therefore, polarization control of the photovoltaic effect can be realized *via* applying different poling voltages. Fig. 10 describes the relationship between photocurrent and polarization in high-quality PZT (Zr/Ti = 20/80) thin films. As can be clearly seen, both photocurrent and polarization show similar hysteresis behaviour, and the photocurrent magnitude depends on the polarization magnitude whereas the sign of photocurrent depends on the polarization direction.

3.2.2 Bandgap and optical absorption. Wide bandgaps and small optical absorption coefficients are the critical shortcomings of ferroelectric oxide perovskites for photovoltaic applications. The bandgaps of some conventional ferroelectric oxide perovskites, such as LNO, BTO and PZT, are all larger than 3 eV.[145–147] Because the bandgap of an oxide perovskite is mainly determined by the B cation d states at the CBM and the O 2p states at the VBM, the large electronegativity differences between conventional B cations (such as Ti^{4+}, Zr^{4+} and Nb^{5+} with a d^0 electron configuration) and the oxygen lead to wide bandgaps. The bandgap can be narrowed in some multiferroic oxides, such as BFO, owing to the presence of partially filled d orbitals in Fe^{3+}. The bandgap of BFO was measured to be 2.2 eV for the single crystal[31] and 2.7 eV for thin film,[32] which still far exceeds the ideal bandgap of 1.34 eV.

The wide bandgap gives rise to a very limited active range of absorption of sunlight. Perovskites with bandgaps larger than 3 eV can therefore only harvest UV light, and unfortunately photons with wavelengths less than 400 nm only account for 3.5% of the solar spectrum. Even for BFO with a bandgap of 2.2 eV, only 25% of the solar energy can be absorbed. In addition, the small absorption coefficient further weakens the light harvesting capability of ferroelectric oxide perovskites. The absorption coefficients at 400 nm of BFO[148] and PZT[149] are 10^4 to 10^5 cm^{-1}, whereas those of BTO[150] and LNO[145] are only 10–100 cm^{-1}. The absorption coefficients will become even lower in the visible range.

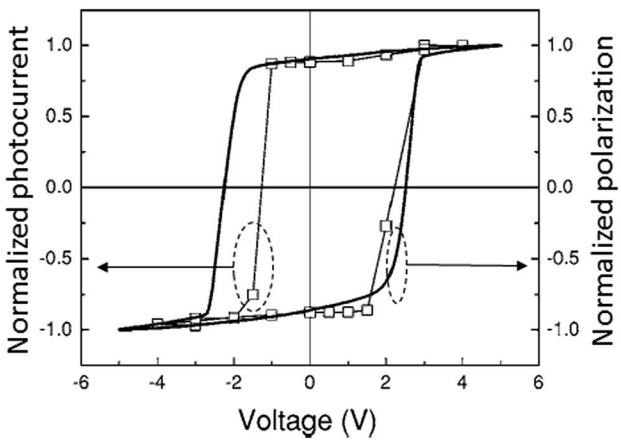

Fig. 10 Hysteresis loops of photocurrent and polarization as a function of poling voltage measured for high quality PZT (Zr/Ti = 20/80) thin films. Reproduced from ref. 144, Copyright 2007, AIP Publishing LLC.

To improve the light harvesting ability, the development of new ferroelectric oxide perovskites with narrowed bandgap and enhanced visible light absorption is crucial. Conspicuous success in bandgap engineering has been recently achieved in Bi_2FeCrO_6 (BFCO) double perovskites[34] and $[KNbO_3]_{1-x}[BaNi_{1/2}Nb_{1/2}O_{3-\delta}]_x$ (KBNNO) perovskite solid solutions.[151] An early theoretical study predicted that ordered BFCO with lattice planes of Fe and Cr ions alternating along the [111] direction could have a bandgap as low as ~1.5 eV.[152] A recent experimental study successfully demonstrated that by tailoring the Fe/Cr cationic ordering and the domain size, the bandgap could be tuned due to the modification of B–O bonding.[34] As shown in Fig. 11a, increasing the Fe/Cr cationic ordering parameter (R) extends the absorption spectra of BFCO into the regions with longer wavelengths and also enhances the absorption coefficient. Enlarging the domain size (D) can also reduce the bandgap (results not shown here). The combined effects of R and D can lead to a tunable bandgap with the minimum value of 1.4 eV. Authors in ref. 34 further fabricated a multilayer thin-film solar cell with different BFCO layers having different R and D, which exhibited significantly enhanced light absorption because of the superposition of absorption peaks of different layers. This multilayer device demonstrated an unprecedentedly high efficiency of 8.1%, setting a new record of photovoltaic efficiency achieved in ferroelectric oxide perovskites. Another successful example of bandgap engineering in ferroelectric oxide perovskites was reported in ref. 151, where a KBNNO perovskite solid solution system was used. The novel idea was that $KNbO_3$ provided ferroelectricity while the Ni^{2+} and the oxygen vacancy from $BaNi_{1/2}Nb_{1/2}O_{3-\delta}$ created in-gap states for $KNbO_3$ to narrow the bandgap. A similar strategy was previously implemented to a non-perovskite ferroelectric $Bi_4Ti_3O_{12}$–$LaCoO_3$ system, and was demonstrated to be effective.[153] Fig. 11b shows that a wide variation of bandgaps in the range of 1.1–3.8 eV is achieved as the amount of $BaNi_{1/2}Nb_{1/2}O_{3-\delta}$ varies from 0 to 50 percent. However, because the KBNNO samples were in the form of ceramics, the measured photocurrent was quite low and far from satisfactory, only in the order of 0.1 μA cm^{-2}. Nevertheless, improved photovoltaic performance in KBNNO high-quality thin films is expected and will undoubtedly arouse considerable research interest.

Other approaches like strain engineering of oxide perovskites may also be employed for bandgap tuning.[154–156]

3.2.3 Electrical conductivity. An oxide perovskite with good ferroelectricity always has a low conductivity, mostly less than 10^{-9} Ω^{-1} cm^{-1}; otherwise the conductive leakage behavior will dominate over the capacitive ferroelectric behavior. Even under the circumstance of illumination, the electrical conductivity can only be enhanced by one or two orders of magnitude, which is still quite low.[148,157] The poor electrical conductivity is detrimental to the photovoltaic charge transport. Improving the conductivity is therefore imperative for an efficient photovoltaic effect in oxide perovskites. Unfortunately, improving the conductivity will inevitably increase the leakage current, which suppresses the ferroelectric polarization switching, and thus only a small remnant polarization is achieved for the separation of photoexcited charge carriers. A tradeoff between conductivity and ferroelectricity is crucial to enhance the overall photovoltaic output.

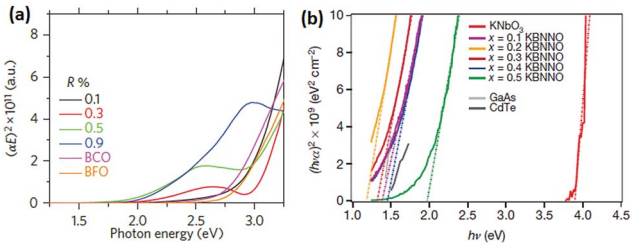

Fig. 11 $(\alpha E)^2$ *vs.* E plot of the UV-vis absorption spectra of (a) BFCO (reproduced from ref. 34, Copyright 2015, Nature Publishing Group) and (b) KBNNO (reproduced from ref. 151, Copyright 2013, Nature Publishing Group).

To modify the conductivity, a good understanding of conduction mechanisms is of great importance. The conduction behaviour in the device comprising a ferroelectric material sandwiched with two electrodes is rather complex, and identifying a specific conduction mechanism can rely on the I–V measurements with different temperatures and sample thicknesses. Generally, there are several possible conduction mechanisms as identified: bulk effects including Ohmic conduction, charge carrier hopping, space charge limited conduction, and Poole–Frenkel emission; and interface effects including Schottky emission and Fowler–Nordheim tunneling.[158] Recent research studies revealed that the conduction through domain walls was much more significant than that within domains, demonstrating an additional conduction mechanism in ferroelectrics.[159,160] In ferroelectric oxide perovskites, particularly, the conduction mechanisms are closely related to oxygen vacancies which can easily form in oxides. For example, two major conduction mechanisms identified in BFO were both correlated with oxygen vacancies: one was the space charge limited conduction with oxygen vacancies as deep traps;[161] and the other one was the Poole–Frenkel emission with Fe^{2+} as trapping centres (note that the valence variation of Fe from +3 to +2 is due to the presence of oxygen vacancies).[162]

According to the conduction mechanisms described above, the ways of tuning the conductivity in oxide perovskites based devices can be either bulk-related or interface-related. Element doping can increase the bulk conductivity of the oxide perovskites and therefore enhance the photocurrent.[163,164] Because the domain walls may be the main conduction channels for photocurrent, the engineering of patterns, orientations and thicknesses of domain walls can manipulate the photovoltaic effect.[33,165,166] The removal of Schottky barriers formed at the ferroelectric/electrode interfaces can facilitate the charge carrier transport and thus promote the photovoltaic charge extraction.[167]

3.3 Photovoltaic mechanisms

Since the first discovery of the anomalous photovoltaic effect in ferroelectric oxide perovskites, many theories have been proposed to account for the origins of this intriguing phenomenon. These theories have different degrees of success

and however so far there is no single theory which can universally explain all the photovoltaic effects observed in ferroelectric oxide perovskites with various forms, such as single crystal, ceramic, single crystalline and polycrystalline thin films. Below we review some widely accepted theories regarding the photovoltaic mechanisms.

3.3.1 Bulk photovoltaic effect. Early studies reported extremely large open-circuit voltage (V_{oc}) in the order of kilovolt in bulk ferroelectrics, such as $LiNbO_3$ (ref. 28) and $BaTiO_3$.[122] Glass *et al.*[29] attributed the origin of the anomalous bulk photovoltaic effect (BPVE) to the non-centrosymmetric nature of ferroelectric crystals. In non-centrosymmetric crystals, the probability of the electron (or hole) transition from the state with the momentum k to a state k' is not equal to the probability of the reverse transition, giving rise to an asymmetric momentum distribution of photoexcited charge carriers.[168] Therefore, a steady short-circuit photocurrent (J_{sc}) is generated and it can be described as:

$$J_{sc} = G\alpha I, \quad (1)$$

where G, α, and I are the Glass coefficient, absorption coefficient, and light intensity, respectively. In the general case where a macroscopic electric field E across the sample is present, the photocurrent is given by:

$$J = J_{sc} - (\sigma_d + \sigma_{ph})E, \quad (2)$$

where σ_d and σ_{ph} are the dark conductivity and photoconductivity, respectively. Under the condition of open-circuit (*i.e.* $J = 0$), V_{oc} can be calculated as:

$$V_{oc} = E_{oc}d = \frac{J_{sc}}{\sigma_d + \sigma_{ph}}d = \frac{G\alpha I}{\sigma_d + \sigma_{ph}}d, \quad (3)$$

where d is the distance between two electrodes. According to eqn (3), V_{oc} is proportional to the distance between two electrodes d and is thus not limited by the bandgap. In addition, when I is small, σ_{ph} can be assumed to be a constant so that V_{oc} increases linearly with I. In the situation where I is large and thus σ_{ph} significantly increases with the I, V_{oc} will become saturated. Eqn (3) can therefore qualitatively explain some early observations of the anomalous photovoltage.

Other observations, such as that photocurrent could even be detected in the direction perpendicular to the polarization vector (*i.e.* the direction of the polar axis),[169–171] indicated that BPVE is a tensorial property. Sturman and Fridkin[172] developed a model of BPVE by using a third-rank tensor to fully describe the relationship between the photocurrent and the incident light. According to their model, eqn (1) can be further expressed as:

$$J_i = I\alpha G_{ijk}e_j e_k, \quad (4)$$

where G_{ijk} is a third-rank tensor of the Glass coefficient, and e_j and e_k are the unit vectors of the projections of the electric field of the linear polarized light along the j^{th} and k^{th} axes, respectively. The product of α and G_{ijk} is often represented by β_{ijk}, which is called the BPVE tensor coefficient. Ji *et al.*[171] compared β_{22} of some typical ferroelectric oxide perovskites at visible wavelengths, and found that β_{22} of BFO was at least five orders of magnitude larger than those of $LiNbO_3$:Fe, $LiTaO_3$ and PLZT. Young *et al.*[166,173] calculated the tensorial BPVE of BTO, PTO and BFO from first-principles by applying the so-called "shift current" theory to their electronic structures, and revealed that the BPVE photocurrent strongly depended on the asymmetric covalent bonding in those ferroelectrics.

Using the tensor expression of BPVE, one can well explain the angular dependence of the photocurrent on the light polarization direction.[168,170] The observation of photocurrent generated in the directions other than the polarization direction also stems from the tensor properties of BPVE. The photocurrent arising from BPVE can show the direction opposite to those arising from other mechanisms. For example, the photocurrent was two orders of magnitude less in BFO (111) film than in (001) film, although both films were sandwiched with the same top and bottom electrodes and both films showed upward polarization.[171] This interesting finding was against the intuition because BFO has the largest polarization along the [111] direction. The reason was attributed to that the photocurrent originating from BPVE greatly cancelled that originating from the depolarization effect in the BFO (111) film.[171] It is expected that when BPVE yields photocurrent with the same direction as those produced by other mechanisms, the overall photovoltaic output will be enhanced.

3.3.2 Depolarization field driven photovoltaic effect. Ferroelectric polarization charges distributed at the two separated surfaces of a ferroelectric material produce a depolarization field (E_{dp}) with the direction opposite to the polarization. The magnitude of E_{dp} is negligible in bulk ferroelectrics because the distance between the two charged surfaces is very large. However, in ferroelectric thin films, the film thickness is usually below a few hundreds of nanometers and therefore the effect of E_{dp} can be significant. The E_{dp} is often blamed for the instability of ferroelectric polarization[174,175] and even the disappearance of ferroelectricity in ultrathin films with the thickness below a few nanometers.[176] Therefore, ferroelectric polarization in thin films can only become stable when the polarization charges are screened by the charge carriers from ferroelectrics themselves or from electrodes. Nevertheless, the polarization charges are normally partially compensated. The residual E_{dp} can thus act as a driving force to separate and transport photoexcited charge carriers. In contrast to the built-in field within the depletion region of a p–n junction, the E_{dp} exists over the whole bulk region of the film. The photocurrent driven by E_{dp} is therefore uniformly distributed within the bulk region of the film, and the measured photovoltaic I–V curves shall be linear, which is different from the diode-like I–V curves arising from some interface photovoltaic effects. Moreover, the E_{dp} model is the most straightforward way to explain the switching of photovoltaic response by manipulating the ferroelectric polarization.[32,144]

Chen[177] first observed the photocurrent with the direction antiparallel to the polarization, and postulated that it was caused by an internal electric field opposite to the polarization although the nature of this internal field was not identified.

This internal field was later assigned to be the E_{dp} resulting from the incomplete screening of ferroelectric polarization charges.[126,128,178] Qin *et al.*[128] established a comprehensive E_{dp} model which simultaneously took into account the ferroelectric polarization, the space charges within the ferroelectric film and the screening charges from electrodes (Fig. 12a), to elucidate how these factors influence the photovoltaic output. Their results showed that both the screening charge distribution and the film thickness could significantly affect the photovoltaic output through influencing the effect of E_{dp}. Because electrodes with high dielectric constants tend to have screen charges distributed away from the interface, using high-dielectric-constant electrodes can weaken the polarization screening effect and thus strengthen the effect of E_{dp}. As shown in Fig. 12b, the combination of Nb:STO and LSMO electrodes with high dielectric constants ($\varepsilon_{Nb:STO} \approx 1000 > \varepsilon_{LSMO} \approx 800 > \varepsilon_{Pt} \approx 8 > \varepsilon_{Au} \approx 6$) gives the highest J_{sc} in PLZT based devices. The photovoltaic performance of PLZT films under extreme conditions, where the dielectric constants of electrodes were infinitely large (*i.e.*, no screening effect) and the widths of space charge regions were zero, was further investigated. Simulation results shown in Fig. 12c reveal that an efficiency as high as 19.5% is possible for PLZT film with the thickness of 1.2 nm (3 unit cells). These theoretically predicted results were exciting and would undoubtedly attract considerable interest in the experimental verifications. Some limitations of this theoretical prediction should be pointed out, such as that poor charge screening will cause polarization instability, and that great leakage current in ultrathin films will lead to a negligible photovoltage. Nevertheless, Qin *et al.*'s studies provide implications, such as using high-dielectric-constant electrodes and reducing the thickness of the ferroelectric layer to enhance the effect of E_{dp}, for the search of high-efficiency photovoltaics in ferroelectric oxide thin films.

3.3.3 Schottky barrier effect. Schottky barrier is an interfacial energy barrier formed when a metal with large work function and a semiconductor (note that common ferroelectric oxide perovskites belong to semiconductors) are brought into contact. The built-in field (E_{bi}) developed at the depletion region near the interface is responsible for the separation of photo-excited electron–hole pairs, and the output photovoltage is determined by the barrier height which is limited by the bandgap of the ferroelectric material. Early studies on bulk ferroelectrics did not take the Schottky barrier effect into account, because the width of the depletion region was much less than the size of the bulk sample and the observed above-bandgap photovoltage could not be explained by the Schottky barrier effect. However, in ferroelectric thin films, the Schottky barrier induced photovoltaic effect may become significant because the width of the depletion region is comparable to the film thickness.

A typical electrode/ferroelectric/electrode sandwich structure can be considered as a back-to-back connection of two Schottky diodes. The magnitude and the direction of the overall photovoltage induced by the Schottky barrier effect depend on the difference between top and bottom barrier heights.[143] The switchable photovoltaic effect can be explained using the knowledge of tunable Schottky barriers, as the barrier height and the depletion width can be modulated by either ferroelectric polarization charge[164,179–181] or charged defects.[131,182] The former mechanism of modulation of Schottky barriers by ferroelectric polarization has been widely investigated, and it was first studied in an Au/PTO/$La_{0.5}Sr_{0.5}CoO_3$ heterostructure.[183] It was observed that by switching polarization, the Au/PTO contact changed from a Schottky-like contact to an Ohmic-like contact, leading to a bistable conduction behavior with an on/off ratio of about two orders of magnitude. The latter mechanism of the modulation of Schottky barriers by charged defects was reported in some defect-rich samples, and those most likely defects were oxygen vacancies because they could easily form in oxide perovskites.[131,182] Note that this defect-involved mechanism in oxide perovskites is analogous to that proposed in organic–inorganic halide perovskites.[25,26] Unlike the ferroelectric

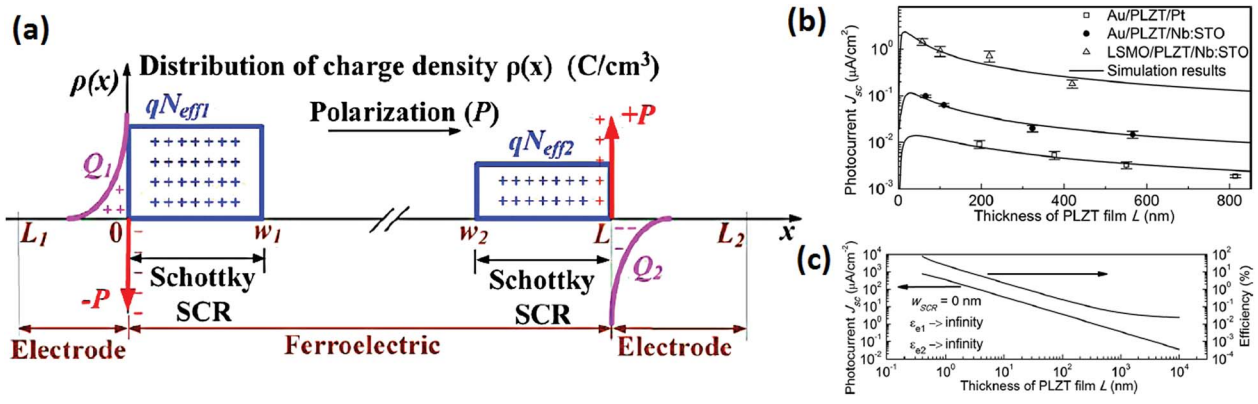

Fig. 12 (a) Charge distribution in an electrode/ferroelectric/electrode sandwiched structure. Polarization charges of $+P$ and $-P$ are located at interfaces of $x = L$ and 0, respectively. Screening charges Q_1 and Q_2 are distributed within the electrodes with finite lengths. Space charges qN_{eff1} and qN_{eff2} are uniformly distributed within regions of $0 < x < w_1$ and $w_2 < x < L$, respectively. (b) Experimentally measured and simulated J_{sc} as a function of film thickness in the LSMO/PLZT/Nb:STO, Au/PLZT/Nb:STO, and Au/PLZT/Pt devices. (c) Simulation results for thickness-dependent J_{sc} and photovoltaic efficiency under the extreme condition: $\varepsilon_{e1} \rightarrow \infty$, $\varepsilon_{e2} \rightarrow \infty$, and $w_{SCR} = 0$. Reproduced from ref. 128, Copyright 2009, AIP Publishing LLC.

polarization switching which can be manipulated by a high-frequency (short-duration) electric pulse with amplitude larger than the coercive field (E_c), the electromigration of oxygen vacancies does not require a poling electric field larger than E_c and however takes a much longer period of time for poling. Moreover, the poled state of oxygen vacancies is unstable after removing the electric field, and thus the associated photovoltaic effect is not stable. These differences can be used to distinguish whether the ferroelectric polarization switching or the electromigration of charged defects is working for the modulation of Schottky barriers.

As reviewed above, both the bulk effect of E_{dp} and the interface effect of the Schottky barrier are related to ferroelectric polarization, and both of them can lead to a switchable photovoltaic effect. Therefore, the mechanism how the switchable photovoltaic effect is controlled by the ferroelectric polarization is still controversial. Perhaps checking the dark conduction behavior simultaneously with the photovoltaic behavior is useful to identify which mechanism is working, because tunable Schottky barriers will give rise to switchable diode-like rectifying behavior in the dark[131,164,183] while the bulk effect of E_{dp} will not.[32]

A proper design of the energy band alignment in the electrode/ferroelectric/electrode sandwich structure can lead to an overall E_{bi} within Schottky barriers having the same direction with E_{dp}.[164] Thus, both E_{bi} and E_{dp} can constructively contribute to the overall photovoltaic output.

3.3.4 Domain wall theory. Recently, Yang *et al.*[33] discovered a fundamentally new mechanism for photovoltaic charge separation, which relied on the electrostatic potential steps at the nanoscale ferroelectric domain walls. Using the model ferroelectric oxide BFO, they observed a large photovoltage (up to 16 V) with in-plane electrodes oriented parallel to domain walls (Fig. 13a and c) and a vanished photovoltaic effect with in-plane electrodes oriented perpendicular to domain walls (Fig. 13b and d). Previous *ab initio* calculations demonstrated the existence of built-in potential steps at domain walls, arising from the component of polarization perpendicular to the domain wall. The theoretical potential steps of BFO 109° and 71° domain walls were 0.15 V and 0.02 V, respectively.[159] Based on these calculations and their experimental observations, authors in ref. 33 and 165 proposed a model regarding potential steps at domain walls as the driving force for charge separation (Fig. 13e). In the dark, a large electric field (~50 kV cm^{-1}) will be formed within the domain wall, and the potential step causes the offset of the conduction band and valence band (Fig. 13f). As a consequence, the overall band exhibits a zigzag shape. Upon illumination, charge carriers excited within domain walls are effectively separated by the built-in field and drift to either side of the domain wall. On the other hand, the photo-generated excitons within domains are highly localized and tightly bounded, and tend to recombine quickly. A net imbalance of charge carriers near the domain wall is thus created and the band structure is significantly tilted (Fig. 13g and h). Therefore, a net overall photovoltage is generated and it results from the additive effect of the potential step across each domain wall. This mechanism could also explain the observed linear increase of

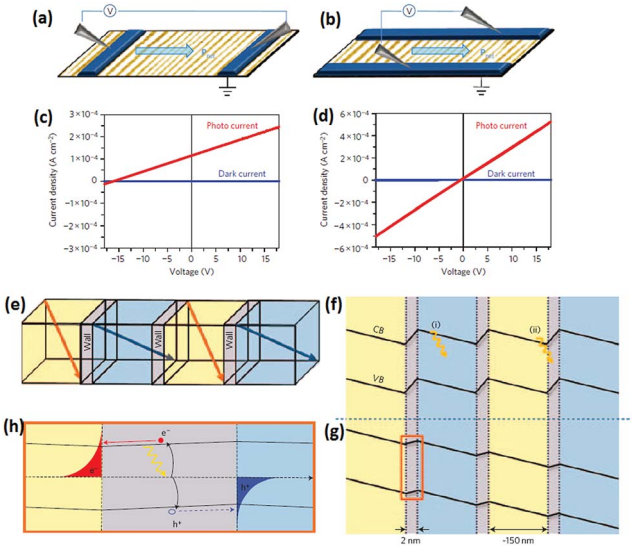

Fig. 13 Schematics showing the orientation of electrodes (a) parallel and (b) perpendicular to domain walls. Corresponding *I*–*V* measurements of devices with (c) parallel and (b) perpendicular electrode configurations. (e) Schematic of 71° domain walls of BFO. Corresponding band diagrams (f) in the dark and (g) under illumination. (h) Detailed picture showing the build-up of photoexcited charge carriers near domain walls. Reproduced from ref. 33, Copyright 2010, Nature Publishing Group.

the output photovoltage with the electrode spacing (*i.e.* the total number of domain walls).[33]

The domain wall theory is fascinating, as it offers the possibility to develop a completely new class of devices in which a tiny volume of a material can generate appreciable photovoltaic effect. However, this hypothesized mechanism still remains questionable, because it could not satisfactorily explain some later experimental findings as listed below. First, BFO single-domain-structured thin films, which do not have domain walls, exhibited above-bandgap photovoltage.[184] Second, BFO thin films with periodic domain structures (both 71° and 109° domains), showed angular dependency of photocurrent on the incident light polarization.[157] Third, all BFO thin films were able to produce above-bandgap photovoltage at low temperature, irrespective of the domain structures and the electrode orientations.[157] Fourth, using photoelectric atomic force microscopy (PhAFM) combined with piezoresponse force microscopy (PFM), Alexe *et al.*[130,185] showed that the non-equilibrium photoexcited charge carriers were almost uniformly generated over the entire BFO crystal, and the generation and recombination lifetimes were large (~35 μs for generation and ~75 μs for recombination) and were not significantly different within domains compared to domain walls. They further suggested that the complex generation and recombination processes were primarily affected by defect-related shallow energy levels, while the domain walls did not play a major role. Finally, based on the above observations, Alexe *et al.*[157] proposed that the origin of the anomalous photovoltaic effect in BFO and analogous ferroelectric oxide perovskites was BPVE rather than the domain wall effect. The role of domain walls was only to provide higher

density of non-equilibrium photoexcited charge carriers because of the high photoconductivity of domain walls. Unfortunately, according to eqn (3), the high dark and photoconductivities of domain walls were detrimental to the V_{oc}. This could explain why in the geometry of electrodes perpendicular to domain walls (Fig. 13b), where conductive domain walls were directly connected to electrodes, a negligible V_{oc} was measured (Fig. 13d). However, when the temperature was lowered, the conductivity of domain walls dropped and thus a remarkable V_{oc} could also be measured in this particular geometry.[157]

4. Open questions and future prospects

Despite the recent tremendous progress made in organic–inorganic metal halide perovskite materials and devices for photovoltaic applications, there are challenges remaining to be overcome in order to commercialize this technology. (1) The champion cells reported so far are unanimously based on organic–inorganic lead halide perovskites. The use of highly toxic and carcinogenic lead element brings concerns on its impact on health and the environment. Fortunately a number of elements have been identified for the substitution of lead, such as Sn, Cu and Fe. But the success in achieving highly efficient perovskite solar cells with these benign elements is still yet to come. (2) Due to the hydroscopic nature of organo-halide salts, *e.g.* methylammonium iodide, the organic–inorganic metal halide perovskite is susceptible to decomposition upon intake of moisture and oxygen. Thus, the instability of the core material in perovskite solar cells requires stringent encapsulation materials and techniques, which will definitely add on the cost and weaken the competitiveness of this novel technology. (3) Compared with silicon-based solar cells, the current state of the art of perovskite solar cells is limited by light absorption. The absorption edge of the best perovskite solar cells is around 800 nm, while that of silicon solar cells is extended to 1100 nm. Although the absorption range can be potentially extended to the near infra-red range *via* bandgap engineering, and some pioneer studies have demonstrated the synthesis of low-bandgap perovskite materials, efficient and stable perovskite solar cells with such low-bandgap perovskite absorbers are still lacking. (4) After a number of observations and experimental measurements, it is universally acknowledged that partial substitution of iodine in $MAPbI_3$ with other halogens such as Cl or Br can greatly improve the charge diffusion length in the perovskite material. Unfortunately the mechanism behind such a phenomenon seems to be missing. The fundamental understanding will pave the way for the development of more superior perovskite materials for photovoltaic cells, as well as for many other opto-electronic applications. (5) Very recently, an increasing number of studies have pointed to ion migration as an important transport phenomenon in halide perovskites.[25,26,186–189] The ion migration and subsequent accumulation near the electrodes cause significant band bending and thus influence the extraction of photogenerated charge carriers. Although the ion migration can be associated with many anomalous properties of halide perovskites, such as slow photoconductivity response, *J–V* hysteresis, and switchable photovoltaic effect, the nature of the ionic species and the dynamics and kinetics of ion migration (*e.g.* activation energies and timescales) are largely unknown and yet to be further investigated.

For ferroelectric oxide perovskites, there is still a long way to go to fully elucidate the photovoltaic mechanisms and to further enhance the energy conversion efficiency. (1) The fundamental studies on the charge carrier dynamics were scarce and scattered. For example, using ultrafast optical spectroscopy, Sheu *et al.*[190] found that the generation of charge carriers in BFO was within a few ps and the lifetime was ~3 ns. Alexe *et al.*[185] reported that both generation and recombination processes in BFO took a few tens of μs because shallow trapping levels were involved in these two processes. In addition, many parameters of charge carrier dynamics, such as mobility and diffusion length, remain largely unknown because they are difficult to measure in the relatively insulating ferroelectric systems. More research on the charge carrier dynamics in ferroelectric oxide perovskites is therefore desired for both fundamental understanding and practical device design. (2) Although in the mechanisms of both BPVE and the E_{dp} model, ferroelectricity plays a crucial role, its dynamics during the photovoltaic process is unclear. Recently, using time-resolved X-ray scattering, Daranciang *et al.*[191] revealed that under the influence of photoexcited charge carriers, the ferroelectricity of PTO could be suppressed and the E_{dp} could even be completely screened. The persistence of ferroelectricity during the photovoltaic process is therefore an issue and has been seldom considered in previous studies. This issue will inevitably lead to the question how ferroelectricity really functions during the photovoltaic process, especially in the case where abundant photoexcited charge carriers are present.[192] This issue is therefore of great necessity to be clarified in the future. (3) To enhance the photovoltaic efficiency, developing new oxide perovskites with narrowed bandgap, improved conductivity, satisfactory polarization magnitude, and engineered domain walls, is promising. We have reason to believe that the currently most-studied BFO is probably only the tip of the iceberg in the vast amount of ferroelectric oxide perovskites for photovoltaics, because of the existing good examples, such as BFCO[34] and KBNNO.[151] It is also promising to combine ferroelectric oxide perovskites with other photoactive semiconductors, *e.g.* organic–inorganic halide perovskites, to achieve greater photovoltaic efficiency,[192–194] because the strong intrinsic dipoles of ferroelectric oxide perovskites can provide the driving force for charge separation and generation, while the photoactive semiconductors are efficient for charge generation and transport. Their combination requires an ingenious design of nanostructured devices, *e.g.*, nanoparticles of ferroelectric oxide perovskites functioning as nanodipoles embedded into photoactive semiconductor matrices. (4) Ferroelectric oxide perovskites do not necessarily need to compete with other photoactive semiconductors, such as organic–inorganic halide perovskites, in terms of energy conversion efficiency, as their potential photovoltaic applications are not restricted to solar

cells, but can be extended to opto-electronic memory,[30] photo-actuators,[35] photo-sensors and dosimeters,[36] and even junction devices showing spin-polarized photocurrent.[37] Other new functionalities are yet to be tapped and exploited in future studies.

5. Conclusions

In summary, we review two important subclasses of perovskites, *i.e.* organic–inorganic halide perovskites and ferroelectric oxide perovskites, for photovoltaic applications, focusing on the material nature and the photovoltaic mechanisms. Each of these two different subclasses of perovskites has its own merits as a photovoltaic material. Organic–inorganic halide perovskites have distinct advantages in light absorption and charge transport, due to their appropriate bandgap, high absorption coefficient, long and balanced electron–hole diffusion lengths, and large dielectric constant. These unique properties enable organic–inorganic halide perovskites adapt to a variety of solar cell architectures, in most of which high efficiencies above 10% have been achieved. Interestingly, different mechanisms have been found to be associated with different solar cell structures based on organic–inorganic halide perovskites. On the other hand, ferroelectric oxide perovskites have shown many intriguing photovoltaic phenomena, such as above-bandgap photovoltage, switchable photocurrent, and photovoltaic charge generation and separation occurring at nanoscale domain walls, all of which can be related to their unique property — ferroelectricity. However, other properties of ferroelectric oxide perovskites, like light absorption and electrical conductivity, are poor and thus need urgent improvement for enhanced photovoltaic performance. Great success of bandgap engineering in ferroelectric oxide perovskites has been achieved and highlighted in this review. The photovoltaic mechanisms in ferroelectric oxide perovskites, however, are not well understood and still controversial in several ways. Finally, we do expect that both subclasses of perovskites will find their respective applications in the field of photovoltaics.

Acknowledgements

Z.F. and J.W. acknowledge the support for research from the Agency for Science, Technology and Research (A*Star) (grant no. 1121202013) and Singapore Ministry of Education (MOE2012-T2-2-102), conducted at the National University of Singapore. K.S. acknowledges Chongqing University for start-up funds under the "One Hundred Talent" Programme (0212001104431).

Notes and references

1 J. Gong, S. B. Darling and F. You, *Energy Environ. Sci.*, 2015, **8**, 1953–1968.
2 B. O'Regan and M. Grätzel, *Nature*, 1991, **353**, 737–740.
3 K. Sun, B. Fan and J. Ouyang, *J. Phys. Chem. C*, 2010, **114**, 4237–4244.
4 Y. Liu, J. R. Jennings, S. M. Zakeeruddin, M. Grätzel and Q. Wang, *J. Am. Chem. Soc.*, 2013, **135**, 3939–3952.
5 F. Li, J. R. Jennings and Q. Wang, *ACS Nano*, 2013, **7**, 8233–8242.
6 F. Li, J. R. Jennings, X. Z. Wang, L. Fan, Z. Y. Koh, H. Yu, L. Yan and Q. Wang, *J. Phys. Chem. C*, 2014, **118**, 17153–17159.
7 G. Li, R. Zhu and Y. Yang, *Nat. Photonics*, 2012, **6**, 153–161.
8 K. Sun, H. M. Zhang and J. Ouyang, *J. Mater. Chem.*, 2011, **21**, 18339–18346.
9 K. Sun and J. Ouyang, *Sol. Energy Mater. Sol. Cells*, 2012, **96**, 238–243.
10 V. Murugesan, K. Sun and J. Ouyang, *Appl. Phys. Lett.*, 2013, **102**, 083302.
11 L. Chen, D. Du, K. Sun, J. Hou and J. Ouyang, *ACS Appl. Mater. Interfaces*, 2014, **6**, 22334–22342.
12 Y. Sun, G. C. Welch, W. L. Leong, C. J. Takacs, G. C. Bazan and A. J. Heeger, *Nat. Mater.*, 2012, **11**, 44–48.
13 H. H. Dam, K. Sun, E. Hanssen, J. M. White, T. Marszalek, W. Pisula, J. Czolk, J. Ludwig, A. Colsmann, M. Pfaff, D. Gerthsen, W. W. H. Wong and D. J. Jones, *ACS Appl. Mater. Interfaces*, 2014, **6**, 8824–8835.
14 K. Sun, Z. Xiao, E. Hanssen, M. F. Klein, H. H. Dam, M. Pfaff, D. Certhsen, W. W. H. Wong and D. J. Jones, *J. Mater. Chem. A*, 2014, **2**, 9048–9054.
15 K. Sun, Z. Xiao, S. Lu, W. Zajaczkowski, W. Pisula, E. Hanssen, J. M. White, R. M. Williamson, J. Subbiah, J. Ouyang, A. B. Holmes, W. W. H. Wong and D. J. Jones, *Nat. Commun.*, 2015, **6**, 6013.
16 P. V. Kamat, *J. Phys. Chem. C*, 2008, **112**, 18737–18753.
17 L. Sun, Z. Y. Koh and Q. Wang, *Adv. Mater.*, 2013, **25**, 4598–4604.
18 L. Sun and Q. Wang, *ACS Appl. Mater. Interfaces*, 2014, **6**, 14239–14246.
19 C. Shen, L. Sun, Z. Y. Koh and Q. Wang, *J. Mater. Chem. A*, 2014, **2**, 2807–2813.
20 N. G. Park, *J. Phys. Chem. Lett.*, 2013, **4**, 2423–2429.
21 Y. Yuan, Z. Xiao, B. Yang and J. Huang, *J. Mater. Chem. A*, 2014, **2**, 6027–6041.
22 A. Kojima, K. Teshima, Y. Shirai and T. Miyasaka, *J. Am. Chem. Soc.*, 2009, **131**, 6050–6051.
23 H. S. Kim, C. R. Lee, J. H. Im, K. B. Lee, T. Moehl, A. Marchioro, S. J. Moon, R. Humphry-Baker, J. H. Yum, J. E. Moser, M. Grätzel and N. G. Park, *Sci. Rep.*, 2012, **2**, 591.
24 W. S. Yang, J. H. Noh, N. J. Jeon, Y. C. Kim, S. Ryu, J. Seo and S. I. Seok, *Science*, 2015, **348**, 1234–1237.
25 Z. Xiao, Y. Yuan, Y. Shao, Q. Wang, Q. Dong, C. Bi, P. Sharma, A. Gruverman and J. Huang, *Nat. Mater.*, 2015, **14**, 193–198.
26 Y. Zhao, C. Liang, H. Zhang, D. Li, D. Tian, G. Li, X. Jing, W. Zhang, W. Xiao, Q. Liu, F. Zhang and Z. He, *Energy Environ. Sci.*, 2015, **8**, 1256–1260.
27 A. G. Chynoweth, *Phys. Rev.*, 1956, **102**, 705–714.
28 A. Glass, D. von der Linde and T. Negran, *Appl. Phys. Lett.*, 1974, **25**, 233–235.
29 A. M. Glass, D. V. D. linde, D. H. Auston and T. J. Negran, *J. Electron. Mater.*, 1975, **4**, 915–943.
30 R. Guo, L. You, Y. Zhou, Z. S. Lim, X. Zou, L. Chen, R. Ramesh and J. Wang, *Nat. Commun.*, 2013, **4**, 1990.

31 T. Choi, S. Lee, Y. J. Choi, V. Kiryukhin and S. W. Cheong, *Science*, 2009, **324**, 63–66.
32 W. Ji, K. Yao and Y. C. Liang, *Adv. Mater.*, 2010, **22**, 1763–1766.
33 S. Y. Yang, J. Seidel, S. J. Byrnes, P. Shafer, C.-H. Yang, M. D. Rossell, P. Yu, Y.-H. Chu, J. F. Scott, J. W. Ager III, L. W. Martin and R. Ramesh, *Nat. Nanotechnol.*, 2010, **5**, 143–147.
34 R. Nechache, C. Harnagea, S. Li, L. Cardenas, W. Huang, J. Chakrabartty and F. Rosei, *Nat. Photonics*, 2015, **9**, 61–67.
35 K. Uchino, *Acta Mater.*, 1998, **46**, 3745–3753.
36 B. K. Gan, K. Yao, S. C. Lai, Y. F. Chen and P. C. Goh, *IEEE Electron Device Lett.*, 2008, **29**, 1215–1217.
37 H. Huang, *Nat. Photonics*, 2010, **4**, 134–135.
38 V. M. Goldschmidt, *Ber. Dtsch. Chem. Ges.*, 1927, **60**, 1263–1268.
39 N. K. McKinnon, D. C. Reeves and M. H. Akabas, *J. Gen. Physiol.*, 2011, **138**, 453–466.
40 M. A. Green, A. Ho-Baillie and H. J. Snaith, *Nat. Photonics*, 2014, **8**, 506–514.
41 P. Umari, E. Mosconi and F. de Angelis, *Sci. Rep.*, 2014, **4**, 4467.
42 A. Poglitsch and D. Weber, *J. Chem. Phys.*, 1987, **87**, 6373–6378.
43 Y. Kawamura, H. Mashiyama and K. J. Hasebe, *J. Phys. Soc. Jpn.*, 2002, **71**, 1694–1697.
44 C. C. Stoumpos, C. D. Malliakas and M. G. Kanatzidis, *Inorg. Chem.*, 2013, **52**, 9019–9038.
45 T. Baikie, Y. N. Fang, J. M. Kadro, M. Schreyer, F. X. Wei, S. G. Mhaisalkar, M. Grätzel and T. J. White, *J. Mater. Chem. A*, 2013, **1**, 5628–5641.
46 C. Quarti, G. Grancini, E. Mosconi, P. Bruno, J. M. Ball, M. M. Lee, H. J. Snaith, A. Petrozza and F. de Angelis, *J. Phys. Chem. Lett.*, 2014, **5**, 279–284.
47 E. Mosconi, C. Quarti, T. Ivanovska, G. Ruani and F. de Angelis, *Phys. Chem. Chem. Phys.*, 2014, **16**, 16137–16144.
48 G. Grancini, S. Marras, M. Prato, C. Giannini, C. Quarti, F. de Angelis, M. de Bastiani, G. E. Eperon, H. J. Snaith, L. Manna and A. Petrozza, *J. Phys. Chem. Lett.*, 2014, **5**, 3836–3842.
49 W.-J. Yin, J. Yang, J. Kang, Y. Yan and S. Wei, *J. Mater. Chem. A*, 2015, **3**, 8926–8942.
50 W.-J. Yin, T. Shi and Y. Yan, *Appl. Phys. Lett.*, 2014, **104**, 063903.
51 Y. Yamada, T. Nakamura, M. Endo, A. Wakamiya and Y. Kanemitsu, *Appl. Phys. Express*, 2014, **7**, 032302.
52 P. Schulz, E. Edri, S. Kirmayer, G. Hodes, D. Cahen and A. Kahn, *Energy Environ. Sci.*, 2014, **7**, 1377–1381.
53 Y. Wang, T. Gould, J. F. Dobson, H. Zhang, H. Yang, X. Yao and H. Zhao, *Phys. Chem. Chem. Phys.*, 2014, **16**, 1424–1429.
54 E. Mosconi, A. Amat, M. K. Nazeeruddin, M. Grätzel and F. de Angelis, *J. Phys. Chem. C*, 2013, **117**, 13902–13913.
55 J. Even, L. Pedesseau and C. Katan, *Phys. Chem. Chem. Phys.*, 2014, **16**, 8697–8698.
56 J. Even, L. Pedesseau, J. M. Jancu and C. Katan, *J. Phys. Chem. Lett.*, 2013, **4**, 2999–3005.
57 L. Lang, J. H. Yang, H. R. Liu, H. J. Xiang and X. G. Gong, *Phys. Lett. A*, 2014, **378**, 290–293.
58 M. H. Du, *J. Mater. Chem. A*, 2014, **2**, 9091–9098.
59 F. Brivio, K. T. Butler, A. Walsh and M. van Schilfgaarde, *Phys. Rev. B: Condens. Matter Mater. Phys.*, 2014, **89**, 155204.
60 A. Amat, E. Mosconi, E. Ronca, C. Quarti, P. Umari, M. K. Nazeeruddin, M. Grätzel and F. de Angelis, *Nano Lett.*, 2014, **14**, 3608–3616.
61 W.-J. Yin, T. Shi and Y. Yan, *Adv. Mater.*, 2014, **26**, 4653–4658.
62 G. Giorgi, J. I. Fujisawa, H. Segawa and K. Yamashita, *J. Phys. Chem. Lett.*, 2013, **4**, 4213–4216.
63 S. D. Stranks, G. E. Eperon, G. Grancini, C. Menelaou, M. J. P. Alcocer, T. Leijtens, L. M. Herz, A. Petrozza and H. J. Snaith, *Science*, 2013, **342**, 341–344.
64 J. Feng and B. Xiao, *J. Phys. Chem. Lett.*, 2014, **5**, 1278–1282.
65 A. Filippetti and A. Mattoni, *Phys. Rev. B: Condens. Matter Mater. Phys.*, 2014, **89**, 125203.
66 F. Brivio, A. B. Walker and A. Walsh, *APL Mater.*, 2013, **1**, 042111.
67 G. Giorgi, J.-I. Fujisawa, H. Segawa and K. Yamashita, *J. Phys. Chem. C*, 2014, **118**, 12176–12183.
68 W. Schckley and H. J. Queisser, *J. Appl. Phys.*, 1961, **32**, 510–519.
69 T. M. Koh, K. Fu, Y. Fang, S. Chen, T. C. Sum, N. Mathews, S. G. Mhaisalkar, P. P. Boix and T. Baikie, *J. Phys. Chem. C*, 2014, **118**, 16458–16462.
70 Y. Takahashi, R. Obara, Z.-Z. Lin, Y. Takahashi, T. Naito, T. Inabe, S. Ishibashi and K. Terakura, *Dalton Trans.*, 2011, **40**, 5563–5568.
71 L. Dimesso, M. Dimamay, M. Hamburger and W. Jaegerman, *Chem. Mater.*, 2014, **26**, 6762–6770.
72 R. Lindblad, N. K. Jena, B. Philippe, J. Oscarsson, D. Bi, A. Lindblad, S. Mandal, B. Pal, D. D. Sarma, O. Karis, H. Siegbahn, E. M. J. Johansson, M. Odelius and H. Rensmo, *J. Phys. Chem. C*, 2015, **119**, 1818–1825.
73 J. Qiu, Y. Qiu, K. Yan, M. Zhong, C. Mu, H. Yan and S. Yang, *Nanoscale*, 2013, **5**, 3245–3248.
74 S. Colella, E. Mosconi, P. Fedeli, A. Listorti, F. Gazza, F. Orlandi, P. Ferro, T. Besagni, A. Rizzo, G. Calestani, G. Gigli, F. de Angelis and R. Mosca, *Chem. Mater.*, 2013, **25**, 4613–4618.
75 H. Yu, F. Wang, F. Xie, W. Li, J. Chen and N. Zhao, *Adv. Funct. Mater.*, 2014, **24**, 7102–7108.
76 M. I. Dar, N. Arora, P. Gao, S. Ahmad, M. Grätzel and M. K. Nazeeruddin, *Nano Lett.*, 2014, **14**, 6991–6996.
77 M.-F. Xu, H. Zhang, S. Zhang, H. L. Zhu, H.-M. Su, J. Liu, K. S. Wong, L.-S. Liao and W. C. H. Choy, *J. Mater. Chem. A*, 2015, **3**, 14424–14430.
78 S. R. Raga, M.-C. Jung, M. V. Lee, M. R. Leyden, Y. Kato and Y. Qi, *Chem. Mater.*, 2015, **27**, 1597–1603.
79 A. Dualeh, P. Gao, S. I. I. Seok, M. K. Nazeeruddin and M. Grätzel, *Chem. Mater.*, 2015, **26**, 6160–6164.
80 J. H. Im, C. R. Lee, J. W. Lee, S. W. Park and N. G. Park, *Nanoscale*, 2011, **3**, 4088–4093.

81 G. Xing, N. Mathews, S. Sun, S. S. Lim, Y. M. Lam, M. Grätzel, S. Mhaisalkar and T. C. Sum, *Science*, 2013, **342**, 344–347.
82 S. Sun, T. Salim, N. Mathews, M. Duchamp, C. Boothroyd, G. Xing, T. C. Sum and Y. M. Lam, *Energy Environ. Sci.*, 2014, **7**, 399–407.
83 S. D. Wolf, J. Holovsky, S.-J. Moon, P. Löper, B. Niesen, M. Ledinsky, F.-J. Haug, J.-H. Yum and C. Ballif, *J. Phys. Chem. Lett.*, 2014, **5**, 1035–1039.
84 F. Hao, C. C. Stoumpos, R. P. H. Chang and M. G. Kanatzidis, *J. Am. Chem. Soc.*, 2014, **136**, 8094–8099.
85 J. H. Noh, S. H. Im, J. H. Heo, T. N. Mandal and S. I. Seok, *Nano Lett.*, 2013, **13**, 1764–1769.
86 M. M. Lee, J. Teuscher, T. Miyasaka, T. N. Murakami and H. J. Snaith, *Science*, 2012, **338**, 643–647.
87 L. Etgar, P. Gao, Z. S. Xue, Q. Peng, A. K. Chandiran, B. Liu, M. K. Nazeeruddin and M. Grätzel, *J. Am. Chem. Soc.*, 2012, **134**, 17396–17399.
88 J. M. Ball, M. M. Lee, A. Hey and H. J. Snaith, *Energy Environ. Sci.*, 2013, **6**, 1739–1743.
89 M. Liu, M. B. Johnston and H. J. Snaith, *Nature*, 2013, **501**, 395–398.
90 C. Wehrenfennig, G. E. Eperon, M. B. Johnston, H. J. Snaith and L. M. Herz, *Adv. Mater.*, 2014, **26**, 1584–1589.
91 C. S. Ponseca, T. J. Savenije, M. Abdellah, K. Zheng, A. Yartsev, T. Pascher, T. Harlang, P. Chabera, T. Pullerits, A. Stepanov, J.-P. Wolf and V. Sundström, *J. Am. Chem. Soc.*, 2014, **136**, 5189–5192.
92 Q. Wang, Y. Shao, H. Xie, L. Lyu, X. Liu, Y. Gao and J. Huang, *Appl. Phys. Lett.*, 2014, **105**, 163508.
93 M. Hirasawa, T. Ishihara, T. Goto, K. Uchida and N. Miura, *Phys. B*, 1994, **201**, 427–430.
94 N. Onoda-Yamamuro, T. Matsuo and H. Suga, *J. Phys. Chem. Solids*, 1992, **53**, 935–939.
95 E. J. Juarez-Perez, R. S. Sanchez, L. Badia, G. Garcia-Belmonte, Y. S. Kang, I. Mora-Sero and J. Bisquert, *J. Phys. Chem. Lett.*, 2014, **5**, 2390–2394.
96 T. M. Clarke and J. R. Durrant, *Chem. Rev.*, 2010, **110**, 6736–6767.
97 I. Strzalkowski, S. Joshi and C. R. Crowell, *Appl. Phys. Lett.*, 1976, **28**, 350–352.
98 J. M. Frost, K. T. Butler, F. Brivio, C. H. Hendon, M. van Schilfgaarde and A. Walsh, *Nano Lett.*, 2014, **14**, 2584–2590.
99 S. Liu, F. Zheng, N. Z. Koocher, H. Takenaka, F. Wang and A. M. Rappe, *J. Phys. Chem. Lett.*, 2015, **6**, 693–699.
100 E. Unger, E. Hoke, C. Bailie, W. Nguyen, A. Bowring, T. Heumüller, M. Christoforo and M. McGehee, *Energy Environ. Sci.*, 2014, **7**, 3690–3698.
101 J. Wei, Y. Zhao, H. Li, G. Li, J. Pan, D. Xu, Q. Zhao and D. Yu, *J. Phys. Chem. Lett.*, 2014, **5**, 3937–3945.
102 Z. Fan, J. Xiao, K. Sun, L. Chen, H. Hu, J. Ouyang, K. P. Ong, K. Zeng and J. Wang, *J. Phys. Chem. Lett.*, 2015, **6**, 1155–1161.
103 Y. Kutes, L. Ye, Y. Zhou, S. Pang, B. D. Huey and N. P. Padture, *J. Phys. Chem. Lett.*, 2014, **5**, 3335–3339.
104 Z. Xiao, Y. Yuan, Y. Shao, Q. Wang, Q. Dong, C. Bi, P. Sharma, A. Gruverman and J. Huang, *Nat. Mater.*, 2015, **14**, 193–198.
105 F. Zheng, H. Takenaka, F. Wang, N. Z. Koocher and A. M. Rappe, *J. Phys. Chem. Lett.*, 2015, **6**, 31–37.
106 N. G. Park, *Mater. Today*, 2014, **18**, 65–72.
107 J. Burschka, N. Pellet, S. J. Moon, R. Humphry-Baker, P. Gao, M. K. Nazeeruddin and M. Grätzel, *Nature*, 2013, **499**, 316–320.
108 F. Deschler, M. Price, S. Pathak, L. E. Klintberg, D.-D. Jarausch, R. Higler, S. Hüttner, T. Leijtens, S. D. Stranks, H. J. Snaith, M. Atatüre, R. T. Phillips and R. H. Friend, *J. Phys. Chem. Lett.*, 2014, **5**, 1421–1426.
109 T. C. Sum and N. Mathews, *Energy Environ. Sci.*, 2014, **7**, 2518–2534.
110 J. Kim, S. H. Lee, J. H. Lee and K. H. Hong, *J. Phys. Chem. Lett.*, 2014, **5**, 1312–1317.
111 Y. X. Zhao, A. M. Nardes and K. Zhu, *J. Phys. Chem. Lett.*, 2014, **5**, 490–494.
112 V. Gonzalez-Pedro, E. J. Juarez-Perez, W. S. Arsyad, E. M. Barea, F. Fabregat-Santiago, I. Mora-Sero and J. Bisquert, *Nano Lett.*, 2014, **14**, 888–893.
113 E. Edri, S. Kirmayer, S. Mukhopadhyay, K. Gartsman, G. Hodes and D. Cahen, *Nat. Commun.*, 2014, **5**, 3461.
114 Q. Chen, H. P. Zhou, Z. R. Hong, S. Luo, H. S. Duan, H. H. Wang, Y. S. Liu, G. Li and Y. Yang, *J. Am. Chem. Soc.*, 2014, **136**, 622–625.
115 A. Marchioro, J. Teuscher, D. Friedrich, M. Kunst, R. van de Krol, T. Moehl, M. Grätzel and J.-E. Moser, *Nat. Photonics*, 2014, **8**, 250–255.
116 S. Aharon, S. Gamliel, B. E. Cohen and L. Etgar, *Phys. Chem. Chem. Phys.*, 2014, **16**, 10512–10518.
117 M. A. Pena and J. L. G. Fierro, *Chem. Rev.*, 2001, **101**, 1981–2017.
118 W. Jösch, R. Munser, W. Ruppel and P. Würfel, *Ferroelectrics*, 1978, **21**, 623–625.
119 K. Peithmann, J. Hukriede, K. Buse and E. Krätzig, *Phys. Rev. B: Condens. Matter Mater. Phys.*, 2000, **61**, 4615.
120 H. G. Festl, P. Hertel, E. Krätzig and R. von Baltz, *Phys. Status Solidi B*, 1982, **113**, 157–164.
121 O. F. Schirmer, M. Imlau and C. Merschjann, *Phys. Rev. B: Condens. Matter Mater. Phys.*, 2011, **83**, 165106.
122 P. S. Brody, *J. Solid State Chem.*, 1975, **12**, 193–200.
123 V. S. Dharmadhikari and W. W. Grannemann, *J. Appl. Phys.*, 1982, **53**, 8988–8992.
124 A. Zenkevich, Y. Matveyev, K. Maksimova, R. Gaynutdinov, A. Tolstikhina and V. Fridkin, *Phys. Rev. B: Condens. Matter Mater. Phys.*, 2014, **90**, 161409.
125 P. S. Brody and F. Crowne, *J. Electron. Mater.*, 1975, **4**, 955–971.
126 K. Nonaka, M. Akiyama, C. N. Xu, T. Hagio, M. Komatsu and A. Takase, *Jpn. J. Appl. Phys.*, 2000, **39**, 5144–5145.
127 M. Qin, K. Yao and Y. C. Liang, *Appl. Phys. Lett.*, 2008, **93**, 122904.
128 M. Qin, K. Yao and Y. C. Liang, *Appl. Phys. Lett.*, 2009, **95**, 022912.

129 S. Yang, L. Martin, S. Byrnes, T. Conry, S. Basu, D. Paran, L. Reichertz, J. Ihlefeld, C. Adamo, A. Melville, Y.-H. Chu, C.-H. Yang, J. L. Musfeldt, D. G. Schlom, J. W. Ager III and R. Ramesh, *Appl. Phys. Lett.*, 2009, **95**, 062909.
130 M. Alexe and D. Hesse, *Nat. Commun.*, 2011, **2**, 256.
131 H. T. Yi, T. Choi, S. G. Choi, Y. S. Oh and S. W. Cheong, *Adv. Mater.*, 2011, **23**, 3403–3407.
132 B. Jaffe, W. R. Cook and H. Jaffe, *Piezoelectric Ceramics*, Academic Press, London, 1971, p. 136.
133 R. J. Zeches, M. D. Rossell, J. X. Zhang, A. J. Hatt, Q. He, C. H. Yang, A. Kumar, C. H. Wang, A. Melville, C. Adamo, G. Sheng, Y. H. Chu, J. F. Ihlefeld, R. Erni, C. Ederer, V. Gopalan, L. Q. Chen, D. G. Schlom, N. A. Spaldin, L. W. Martin and R. Ramesh, *Science*, 2009, **326**, 977–980.
134 S.-E. Park and T. R. Shrout, *J. Appl. Phys.*, 1997, **82**, 1804–1811.
135 S. H. Wemple, M. DiDomenico Jr. and I. Camlibel, *Appl. Phys. Lett.*, 1968, **12**, 209–211.
136 H. H. Wieder, *Phys. Rev. B: Solid State*, 1955, **99**, 1161.
137 D. Berlincourt, *Proc. IRE*, 1960, **48**, 220–229.
138 D. Lebeugle, D. Colson, A. Forget and M. Viret, *Appl. Phys. Lett.*, 2007, **91**, 022907.
139 K. J. Choi, M. Biegalski, Y. L. Li, A. Sharan, J. Schubert, R. Uecker, P. Reiche, Y. B. Chen, X. Q. Pan, V. Gopalan, L. Q. Chen, D. G. Schlom and C. B. Eom, *Science*, 2004, **306**, 1005–1009.
140 I. Vrejoiu, G. le Rhun, L. Pintilie, D. Hesse, M. Alexe and U. Gösele, *Adv. Mater.*, 2006, **18**, 1657–1661.
141 J. X. Zhang, Q. He, M. Trassin, W. Luo, D. Yi, M. D. Rossell, P. Yu, L. You, C. H. Wang, C. Y. Kuo, J. T. Heron, Z. Hu, R. J. Zeches, H. J. Lin, A. Tanaka, C. T. Chen, L. H. Tjeng, Y. H. Chu and R. Ramesh, *Phys. Rev. Lett.*, 2011, **107**, 147602.
142 Z. Fan, J. Xiao, H. Liu, P. Yang, Q. Ke, W. Ji, K. Yao, K. P. Ong, K. Y. Zeng and J. Wang, *ACS Appl. Mater. Interfaces*, 2015, **7**, 2648–2653.
143 M. Qin, K. Yao and Y. C. Liang, *J. Appl. Phys.*, 2009, **105**, 061624.
144 L. Pintilie, I. Vrejoiu, G. Le Rhun and M. Alexe, *J. Appl. Phys.*, 2007, **101**, 064109.
145 A. Dhar and A. Mansingh, *J. Appl. Phys.*, 1990, **68**, 5804–5809.
146 S. H. Wemple, *Phys. Rev. B: Solid State*, 1970, **2**, 2679.
147 J. F. Scott, *Jpn. J. Appl. Phys.*, 1999, **38**, 2272–2274.
148 S. Basu, L. Martin, Y. Chu, M. Gajek, R. Ramesh, R. Rai, X. Xu and J. Musfeldt, *Appl. Phys. Lett.*, 2008, **92**, 091905.
149 Y. Jiang, X. Tang, Q. Liu, Q. Li and A. Ding, *Mater. Sci. Eng., B*, 2007, **137**, 304–309.
150 C. Berglund and H. Braun, *Phys. Rev.*, 1967, **164**, 790–799.
151 I. Grinberg, D. V. West, M. Torres, G. Gou, D. M. Stein, L. Wu, G. Chen, E. M. Gallo, A. R. Akbashev, P. K. Davies, J. E. Spanier and A. M. Rappe, *Nature*, 2013, **503**, 509–512.
152 P. Baettig and N. A. Spaldin, *Appl. Phys. Lett.*, 2005, **86**, 012505.
153 W. S. Choi, M. F. Chisholm, D. J. Singh, T. Choi, G. E. Jellison Jr and H. N. Lee, *Nat. Commun.*, 2012, **3**, 689.
154 R. F. Berger, C. J. Fennie and J. B. Neaton, *Phys. Rev. Lett.*, 2011, **107**, 146804.
155 H. L. Liu, M. K. Lin, Y. R. Cai, C. K. Tung and Y. H. Chu, *Appl. Phys. Lett.*, 2013, **103**, 181907.
156 Z. Fan, J. Wang, M. B. Sullivan, A. Huan, D. J. Singh and K. P. Ong, *Sci. Rep.*, 2014, **4**, 4631.
157 A. Bhatnagar, A. R. Chaudhuri, Y. H. Kim, D. Hesse and M. Alexe, *Nat. Commun.*, 2013, **4**, 2835.
158 L. Pintilie, *Charge transport in ferroelectric thin films*, INTECH Open Access Publisher, 2011.
159 J. Seidel, L. W. Martin, Q. He, Q. Zhan, Y. H. Chu, A. Rother, S. Gemming, F. Want, G. Catalan, J. F. Scott, N. A. Spaldin, J. Orensteing and R. Ramesh, *Nat. Mater.*, 2009, **8**, 229–234.
160 J. Guyonnet, I. Gaponenko, S. Gariglio and P. Paruch, *Adv. Mater.*, 2011, **23**, 5377–5382.
161 X. Qi, J. Dho, R. Tomov, M. G. Blamire and J. L. MacManus-Driscoll, *Appl. Phys. Lett.*, 2005, **86**, 062903.
162 G. W. Pabst, L. W. Martin, Y.-H. Chu and R. Ramesh, *Appl. Phys. Lett.*, 2005, **90**, 072902.
163 K. Nonaka, M. Akiyama, C. N. Xu, T. Hagio, M. Komatsu and A. Takase, *Jpn. J. Appl. Phys.*, 2000, **39**, 5144–5145.
164 Z. Fan, W. Ji, T. Li, J. Xiao, P. Yang, K. P. Ong, K. Zeng, K. Yao and J. Wang, *Acta Mater.*, 2015, **88**, 83–90.
165 J. Seidel, D. Fu, S.-Y. Yang, E. Alarcon-Llado, J. Wu, R. Ramesh and J. W. Ager III, *Phys. Rev. Lett.*, 2011, **107**, 126805.
166 S. M. Young, F. Zheng and A. M. Rappe, *Phys. Rev. Lett.*, 2012, **109**, 236601.
167 D. Cao, C. Wang, F. Zheng, W. Dong, L. Fang and M. Shen, *Nano Lett.*, 2012, **12**, 2803–2809.
168 V. M. Fridkin, *Crystallogr. Rep.*, 2001, **46**, 654–658.
169 A. Anikiev, L. G. Reznik, B. S. Umarov and J. F. Scott, *Ferroelectr., Lett. Sect.*, 1985, **3**, 89–96.
170 G. Dalba, Y. Soldo, F. Rocca, V. M. Fridikin and P. Sainctavit, *Phys. Rev. Lett.*, 1995, **74**, 988.
171 W. Ji, K. Yao and Y. C. Liang, *Phys. Rev. B: Condens. Matter Mater. Phys.*, 2011, **84**, 094115.
172 B. I. Sturman and V. M. Fridkin, *The Photovoltaic and Photorefractive Effects in Noncentrosymmetric Materials*, Gordon and Breach Science, 1992.
173 S. M. Young and A. M. Rappe, *Phys. Rev. Lett.*, 2012, **109**, 116601.
174 P. Wurfel, I. P. Batra and J. T. Jacobs, *Phys. Rev. Lett.*, 1973, **30**, 1218.
175 Z. Fan, J. Xiao, K. Yao, K. Zeng and J. Wang, *Appl. Phys. Lett.*, 2015, **106**, 102902.
176 J. Junquera and P. Ghosez, *Nature*, 2003, **422**, 506–509.
177 F. S. Chen, *J. Appl. Phys.*, 1969, **40**, 3389.
178 M. Qin, K. Yao, Y. C. Liang and S. Shannigrahi, *J. Appl. Phys.*, 2007, **101**, 014104.
179 Y. S. Yang, S. J. Lee, S. Yi, B. G. Chae, S. H. Lee, H. J. Joo and M. S. Jang, *Appl. Phys. Lett.*, 2000, **76**, 774.
180 D. Lee, S. H. Baek, T. H. Kim, J. G. Yoon, C. M. Folkman, C. B. Eom and T. W. Noh, *Phys. Rev. B: Condens. Matter Mater. Phys.*, 2011, **84**, 125305.
181 L. Fang, L. You, Y. Zhou, P. Ren, Z. S. Lim and J. Wang, *Appl. Phys. Lett.*, 2014, **104**, 142903.

182 Y. Guo, B. Guo, W. Dong, H. Li and H. Liu, *Nanotechnology*, 2013, **24**, 275201.
183 P. W. M. Blom, R. M. Wolf, J. F. M. Cillessen and M. P. C. M. Krijn, *Phys. Rev. Lett.*, 1994, **73**, 2107.
184 S. Nakashima1, T. Uchida, D. Nakayama, H. Fujisawa, M. Kobune and M. Shimizu1, *Jpn. J. Appl. Phys.*, 2014, **53**, 09PA16.
185 M. Alexe, *Nano Lett.*, 2012, **12**, 2193–2198.
186 Y. Zhang, M. Liu, G. E. Eperon, T. C. Leijtens, D. McMeekin, M. Saliba, W. Zhang, M. de Bastiani, A. Petrozza, L. M. Herz, M. B. Johnston, H. Lin and H. J. Snaith, *Mater. Horiz.*, 2015, **2**, 315–322.
187 J. Beilsten-Edmands, G. E. Eperon, R. D. Johnson, H. J. Snaith and P. G. Radaelli, *Appl. Phys. Lett.*, 2015, **106**, 173502.
188 C. Zhao, B. Chen, X. Qiao, L. Luan, K. Lu and B. Hu, *Adv. Energy Mater.*, 2015, 1500279.
189 J. M. Azpiroz, E. Mosconi, J. Bisquert and F. de Angelis, *Energy Environ. Sci.*, 2015, **8**, 2118–2127.
190 Y. M. Sheu, S. A. Trugman, Y.-S. Park, S. Lee, H. T. Yi, S.-W. Cheong, Q. X. Jia, A. J. Taylor and R. P. Prasankumar, *Appl. Phys. Lett.*, 2012, **100**, 242904.
191 D. Daranciang, M. J. Highland, H. Wen, S. M. Young, N. C. Brandt, H. Y. Hwang, *et al.*, *Phys. Rev. Lett.*, 2012, **108**, 087601.
192 Z. Fan, K. Yao and J. Wang, *Appl. Phys. Lett.*, 2014, **105**, 162903.
193 X. Yang, X. Su, M. Shen, F. Zheng, Y. Xin, L. Zhang, M. Hua, Y. Chen and V. G. Harris, *Adv. Mater.*, 2012, **24**, 1202–1208.
194 P. Zhao, L. Bian, L. Wang, J. Xu and A. Chang, *Appl. Phys. Lett.*, 2014, **105**, 013901.